

Oxide Nanoelectronics

Ferroelectric Memories Nanoscale Size Limits Microwave Devices Josephson Junctions

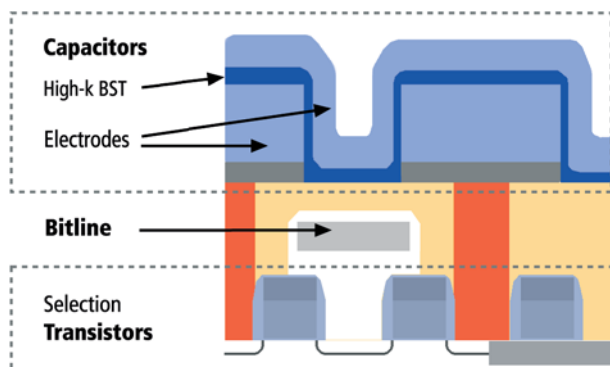
High Permittivity Oxides for DRAM Applications	191
Towards the Limits of Ferroelectricity	197
Finite Size Effects in Ultrathin Ferroelectric Films	202
Imprint Effects in Ferroelectric Thin Films for Memories (FeRAMs)	207
Ferroelectric Thin Films for Integrated Optics	212
Novel Dielectric Structures for Advanced High Frequency Communication and Sensor Systems	216
High-Temperature Superconductor Josephson Multijunction Circuits for Quantum Metrology and Precision Measurements	224
High- T_c Superconducting Magnetometers with Submicro- meter Bicrystal Junctions for Information Technology	230
Terahertz Hilbert Spectroscopy Using Nanoscale High- T_c Josephson Junctions	235





High Permittivity Oxides for DRAM Applications

The fabrication of future nanoscale capacitors of improved performance or for non-volatile memory applications will rely on the thin film technology of complex oxides. Perovskite oxides are prime candidates for these applications, because of their high permittivity in the paraelectric phase or their ferroelectric properties [1]. As an example for a high-k material, we will study the solid solution system $(\text{Ba}_x\text{Sr}_{1-x})\text{TiO}_3$, (BST), which is a candidate for the DRAM manufacturing process, replacing the conventional oxide/nitride/oxide (ONO) dielectrics. The design of such a DRAM cell with an integrated BST thin film capacitor is shown in Fig. 1. Thin films of BST have a high permittivity, between 100-400, compared to 3.9 for pure SiO_2 , thus allowing a simpler design of the cell, if compared to the otherwise necessary complex stack or trench structure. Presently, the permittivity of thin films is still below the values obtained for bulk samples. It is our goal to study, understand, and improve these materials in their thin film form.



TASK

Fig. 1
Schematics of a 1T-1C DRAM cell with stacked high-k capacitor over bitline (COB-design). The dielectric capacitor is located on top of the CMOS transistors. All capacitors have continuous dielectric and top electrode layers. Capacitor and transistor are connected by the red via.

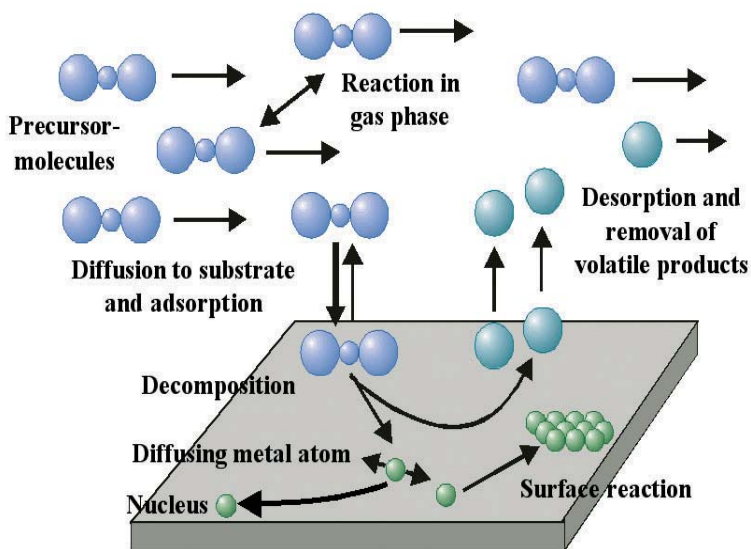
Presently we are developing the deposition of well defined thin oxide films, in particular by the metal-oxide chemical vapor deposition (MOCVD) technique. It is considered as a primary deposition technique for oxide based sub-micrometer or **nanometer** scale devices due to its high deposition rates, its amenability to

Fig. 2
MOCVD planetary reactor
AIX-2600G3 from the
AIXTRON AG, which can
handle five 6" wafers simul-
taneously



large wafer size scaling, and its high thickness conformality over extended device topographies. These samples will permit the pursuit of our second aim, the investigation of their microstructure-property. We will establish a broad database on microstructural, chemical and electrical properties. These data are needed for reliable modeling, understanding and process control of the material microstructure and the resulting electrical performance. In cooperation with AIXTRON AG, Aachen, a new oxide MOCVD deposition system has been installed. It is based on an AIX-

Fig. 3
Schematic of the MOCVD
growth process



2600G3 planetary system (Fig. 2), which can handle five 6-inch wafers simultaneously. This reactor allows the evaluation of MOCVD processes, including the large scale production. A schematic of the growth process is shown in Fig. 3. The fabricated thin films are characterized by numerous analytical methods with special emphasis on the microscopy techniques, as high resolution transmission and scanning electron microscopy (HRTEM, SEM) as well as different types of scanning probe microscopy (SPM). Decisive for the planned applications are the electrical properties. Electrical measurements (permittivity and leakage current, e.g.) are performed for a range of external parameters such as electrode material, temperature, applied field, frequency, etc. For modeling and simulation ab-initio and finite element method calculations are available. Some results on film deposition technology, microstructural and electrical investigations as well as modeling are presented.

Reactor technology

The planetary multi-wafer reactor is presently dedicated to the deposition of high-k ceramic thin films, within the solid solution series $(\text{Ba}_x\text{Sr}_{1-x})\text{TiO}_3$ [2]. Presently, most of the advanced reactors intended for mass production use single wafer showerhead designs. In contrast, we investigate the performance of a batch-processing tool. As one advantage of our reactor design, we obtain precursor incorporation efficiencies which are much higher than those reported for showerhead reactors and, therefore, promise a significant cost advantage as well as a very good thickness homogeneity of the films (see Fig. 4).

Microstructure and surface morphology

At deposition temperatures around 650°C BST films can be grown with a perfect (100) texture on Pt(111) electrodes and clean interfaces as evidenced by the HRTEM micrograph in Fig. 5. Additionally, a columnar structure of the grains is demonstrated by SEM (see Fig. 6).

Stoichiometry control, especially the (Ba+Sr)/Ti ratio, was shown to be a key issue for the control and optimization of the film properties. As an example, Fig. 7 shows that the growth modes and the surface morphology can change drastically with small

RESULTS

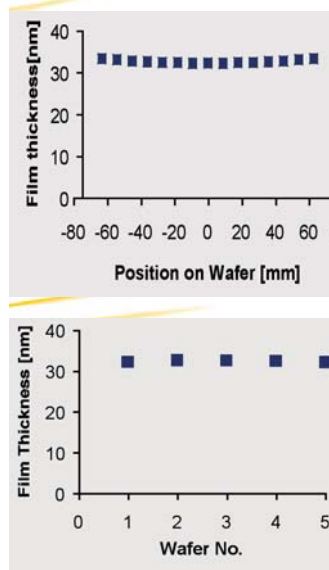


Fig. 4
Homogeneity of the MOCVD
deposition:
(a) across the wafer and
(b) from wafer to wafer



Fig. 5
HRTEM micrograph of the
BST / Pt interface

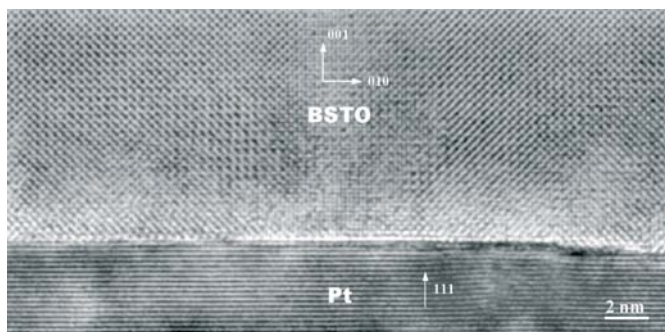


Fig. 6
SEM micrograph showing
the perfect columnar
structure of the BST films

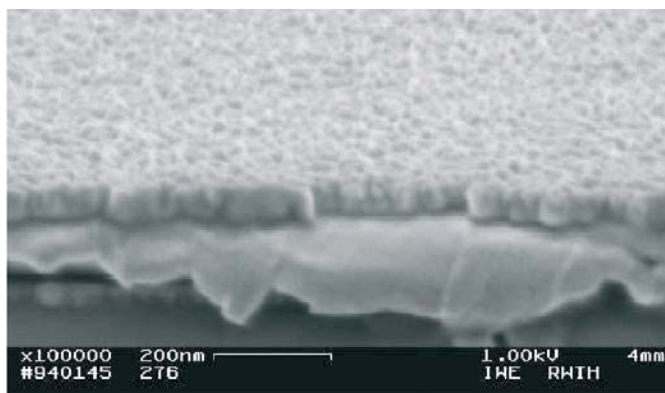
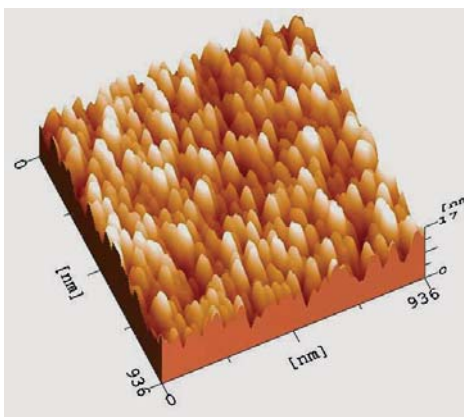
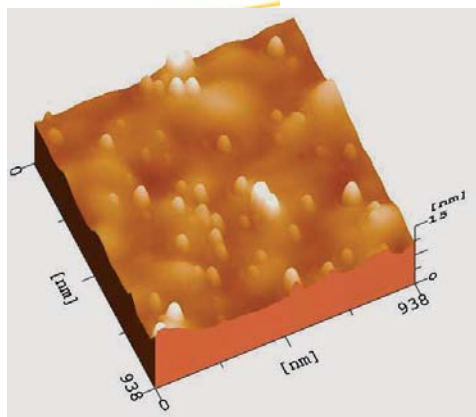


Fig. 7
AFM images of MOCVD BST
films: Ti-rich (left)
and (Ba+Sr)-rich (right).



changes in stoichiometry. These observations are discussed in relation to the different incorporation of excess atoms and to the so-called irregular grain growth observed for Ti-rich bulk ceramics.

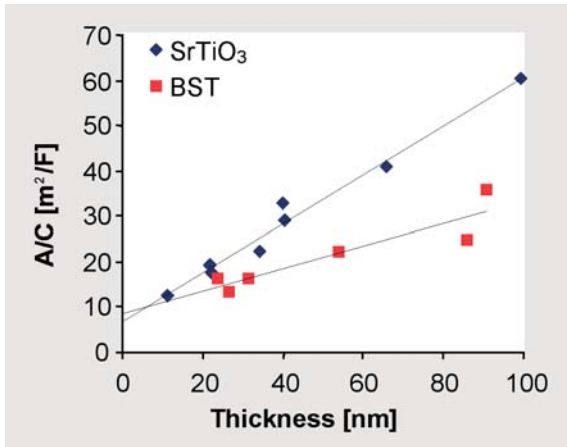


Fig. 8
Reciprocal capacity vs. film thickness for SrTiO₃ and (Ba_{0.7}Sr_{0.3})TiO₃ thin films grown by MOCVD.

Electrical properties

Generally, some dependence of the effective permittivity on thickness, t , is observed in thin films as shown in Fig. 8. For a homogeneous capacitor the inverse capacitance, $1/C$, should be extrapolated to the origin for $t \rightarrow 0$. Instead, a positive intercept is observed. Such behavior can be phenomenologically described by additional thin interface layers ($t_i \ll t$) at the electrodes with a reduced permittivity ($\epsilon_i \ll \epsilon_{\text{BST}}$), so-called “dead” layers [2,3]. Assuming these three capacitances in series – the model is shown in Fig. 9 – the film permittivity, ϵ_{BST} , can be extracted from the slope of the fitted lines. For identical dead layers at both electrodes the intercept delivers the ratio t_i / ϵ_i .

Besides the relaxation in high- k dielectrics leakage of the capacitor is a serious issue for application because high losses by these mechanisms reduce the refresh times for the stored information. For the intended high-Gbit integration the thickness dependence of these properties is most important. As an example, leakage currents in BST thin films between Pt electrodes show a strong dependence on film thickness as demonstrated in Fig. 10. Fig. 10a presents the experimental results for films with a thickness between 20 and 110 nm. The thinnest film shows by far the smallest leakage at all fields while the thickest film is leaking most strongly. This very surprising result can be understood by a model [3]. It takes into account on one hand the field enhanced thermionic emission injection of carriers

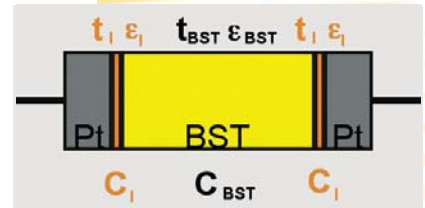


Fig. 9
Three capacitor model of a series connection of the capacities of the BST film and the dead layers at the film interfaces. The resulting reciprocal capacitance is the sum of the individual reciprocal capacitances.

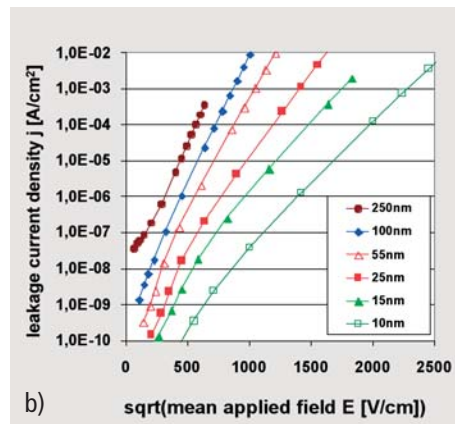
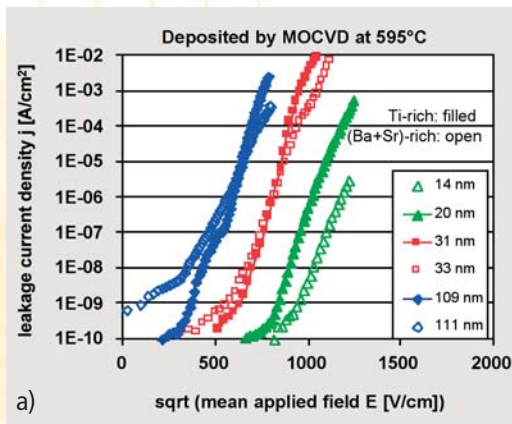


Fig. 10
"Schottky-plot" of the leakage current density j vs. \sqrt{E} (the mean applied field) for Pt / BST / Pt film capacitors of different thickness of the dielectric layer:
a) measured at 300 K
b) model simulation.

(Schottky effect) and the low conductivity of the BST. This is a limiting mechanism for the current. On the other hand, the mentioned three capacitor model with dead layers is responsible for the observed thickness dependence, as the field at the injecting electrode increases with thickness. This increases the injection. Model simulation data [3] presented in Fig. 10b indeed confirm the observed behavior. This example successfully demonstrates the validity of the scientific approach described above.

REFERENCES

- [1] A.I. Kingon, J.P. Maria, and S.K. Streiffer, Alternative dielectrics to SiO_2 for memory and logic devices, *Nature* 406 (2000) 1032
- [2] F. Fitsilis, S. Regnery, P. Ehrhart, R. Waser, F. Schienle, M. Schumacher, and H. Juergensen, Structure Property Relations of BST Thin Films, *Integrated Ferroelectrics* **38** (2001) 855-864
- [3] H. Schroeder, S. Schmitz, and P. Meuffels, Simulation of leakage currents in thin films with dead layers, *Integrated Ferroelectrics*, 47 (2002) 197

AUTHORS

Peter Ehrhart, Herbert Schroeder,
Susanne Hoffmann-Eifert

Towards the Limits of Ferroelectricity

The great interest in high density nanoscale ferroelectric random access memory devices (FeRAMs) leads to the question:

how thin and how small may a ferroelectric film for a capacitor be and still remain stable and switchable?

The transition from the ferroelectric phase to a superparaelectric phase must occur, since ferroelectricity is a collective phenomenon. However, until today only estimates for the size limit are available [1]. It is important to study this limiting size and to evaluate the achievable storage density for future FeRAM devices.

Many experimental studies of size-effects in ferroelectrics use a top-down approach starting with a ferroelectric thin film and then use electron beam or focused ion beam etching methods to create small structures. With the top-down approach it is difficult to distinguish between the intrinsic size effects and the damage related effects induced by the processing. Furthermore, to achieve nanometer size lateral structures a significant experimental effort is required. Up to now the intrinsic ferroelectric limit could not be reached with these methods. For these reasons we propose a bottom-up approach by growing single ferroelectric grains on a silicon substrate. As model material for the perovskites lead titanate (PbTiO_3) thin films are investigated. A chemical solution deposition (CSD) process, designed for the preparation of thin films, is modified to achieve separated single PbTiO_3 grains in a size from 200 nm to less than 20 nm. This method allows to study intrinsic size effects, using a well controlled deposition method without the need of sophisticated lateral patterning.

Our powerful tool for monitoring and manipulation of the nanometer scale domains of these ferroelectric grains is the piezo-response scanning force microscope (PFM). A sketch of the PFM is shown in Fig. 1. During the scanning process of a ferroelectric or piezoelectric thin film, an alternating voltage is applied to the

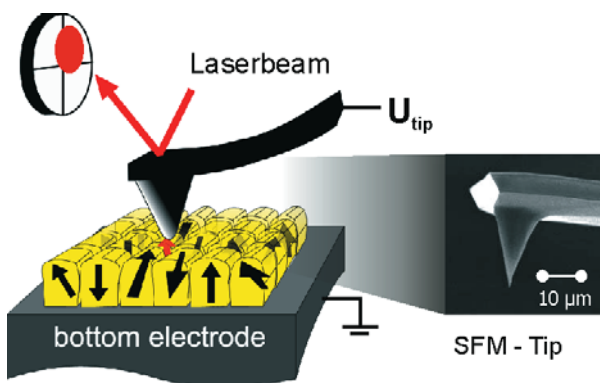
TASK

APPROACH



Fig. 1

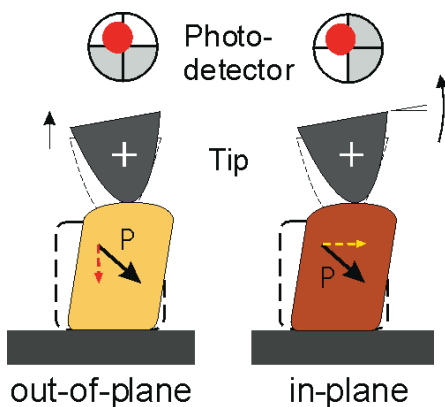
Sketch of the PFM. In contact mode, a conductive cantilever is scanned over a ferroelectric surface while a voltage is applied. The inverse piezoelectric effect of each grain is observed.



conducting cantilever. Due to the piezoelectric effect the thin film is locally deformed. The deformation of the ferroelectric thin film and the orientation of the polarization are linked by the piezoelectric coefficients (see Fig. 2). The PFM permits to monitor simultaneously ferroelectric and topological properties of individual grains.

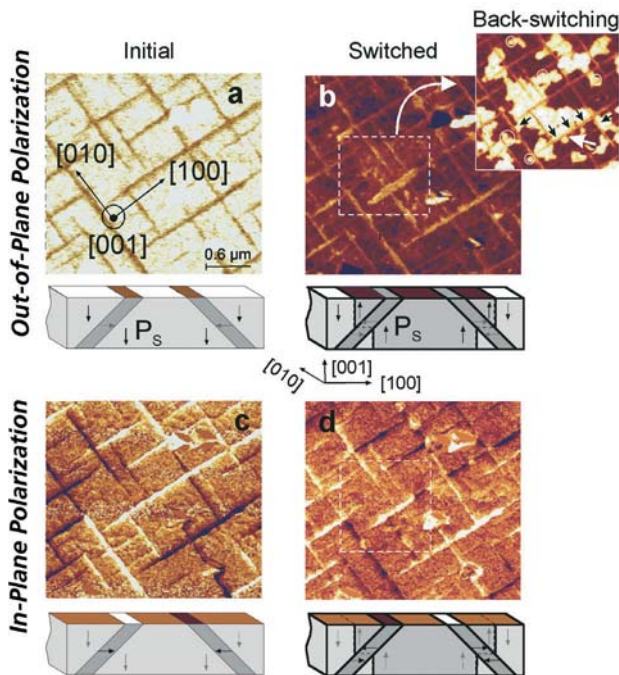
Fig. 2

Principal movement of the cantilever and the reflected laser spot on the four-sector photodiode while applying a voltage to the ferroelectric grain. If the polarization is lying in the x-z-plane (as sketched) the cantilever experiences a lifting (leading to the out-of-plane signal OPP) as well as a torsion denoted as the in-plane signal (IPP).



Switching studies on epitaxial films

An epitaxial $\text{PbZr}_{0.2}\text{Ti}_{0.8}\text{O}_3$ (PZT) thin film was used to study the switching behavior. In Fig. 3(a) and 3(c) the polarization distribution in the as-grown state is displayed. The film is polarized downwards as shown in the sketches below the PFM images. In the second step a scan is performed while applying a dc-voltage of -8 V to the cantilever, which switches the polarization upwards (Fig. 3(b) and (d)). Please note that due to the depolarization field the in-plane polarization is switched by 180° also (compare Fig. 3(c) and (d)). The domain configuration at the domain walls is always head to tail in order to minimize the energy due to surface charges [2].



RESULTS

Fig. 3
Piezoresponse images of an epitaxial poly-domain PZT thin film in the as-grown state, (a) out-of-plane image, (c) in-plane image and after poling (b), (d). Regions with bright, dark, and intermediate contrast correspond to different domains, as shown schematically in the sketches below the PFM images. The inset in (b) shows the region from where the back-switching starts.

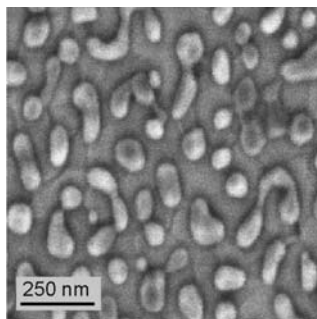
Ferroelectric PbTiO_3 nanograins reaching the size limits

The PTO nanograins were deposited onto $\text{Si}/\text{SiO}_2/\text{TiO}_2/\text{Pt}$ substrates. The separated PbTiO_3 grains have no predominant crystallographic orientation as proven by X-ray diffraction experiments. Fig. 4 shows a scanning electron microscope (SEM) image of a sample with grain sizes in the range of 20 nm to 200 nm.



Fig. 4

SEM image of a PbTiO_3 film consisting of separated single grains in the range of 20 nm to about 200 nm. As substrate a platinized silicon wafer is used.



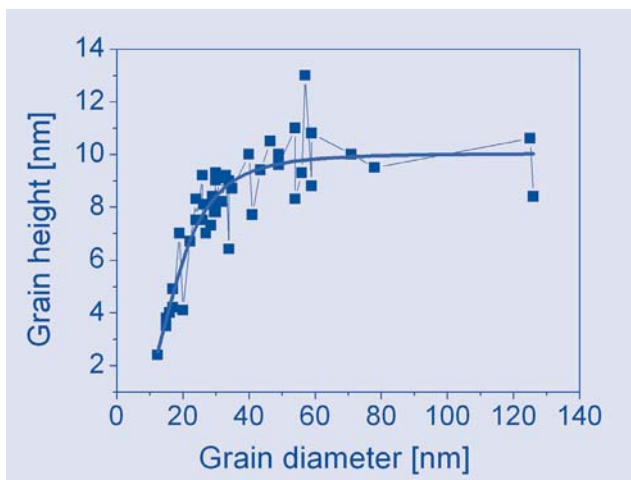
The size and height distribution of the separated PbTiO_3 grains larger than 50 nm shows an average height of 10 nm (Fig. 5). Smaller grains are lower in height. The smallest measured grain had a diameter of about 12 nm and its height was 2.4 nm.

Fig. 5

Grain-height (G_{height}) as a function of grain diameter (G_{diam}). The solid line is the fitted Hill-function

$$G_{\text{height}} = G_{\text{max}} \cdot G_{\text{diam}}^n / (k^n + G_{\text{diam}}^n).$$

For PTO islands larger than 40 nm the average height is 10 nm. The smallest island has a grain-diameter of 12 nm.



Most fascinating is the finding represented in Fig. 6. The topographical image clearly shows eight PbTiO_3 grains. Two of them (marked with the white circles) do not lead to a piezoresponse signal, as shown in the piezoresponse image Fig. 6(b). From the line-scan, the grain sizes are estimated to be about 18 nm. For our samples, at this grain-size the transition from the ferroelectric to the superparaelectric phase could take place [3]. Accordingly a ferroelectric storage capacitor based on these materials should be larger in size than 20 nm.

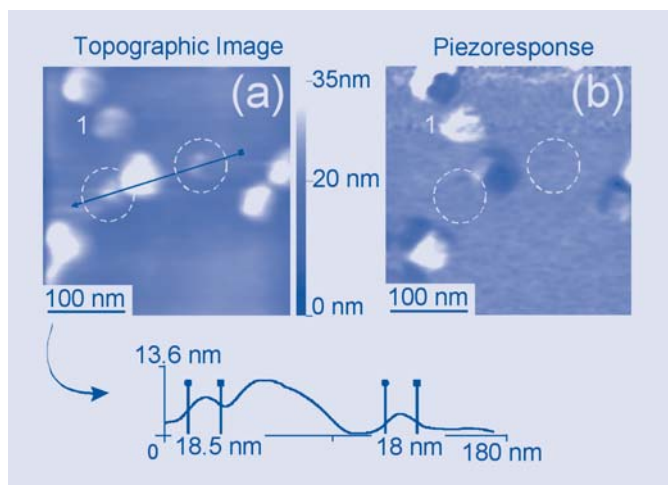


Fig. 6

The topographic image (a) shows eight PbTiO_3 grains of sizes between 100 nm down to less than 20 nm indicated by the circles. From the line-scan over the grains the size of the grains can be determined. In the PFM image (b) the piezoresponse of the grains smaller than 20 nm is not visible leading to the conclusion they do not have any permanent polarization. The smallest grain showing piezoresponse was 30 nm in diameter. It is marked by "1".

- [1] W. L. Zhong, Y. G. Wang, P. L. Zhang, and B. D. Qu, Phys. Rev. B 50, 698 (1994), C. L. Wang and S.P. Smith, J Phys.: Condens. Matter 7, 7163 (1995)
- [2] C. S. Ganpule, B. K. Hill, S. P. Alpay, V. Nagarajan, A. L. Roytburd, E. D. Williams, R. Ramesh, A. Roelofs, R. Waser and L. M. Eng, J. App. Phys., 91, no. 3, 1477-1481, (2002); A. Roelofs, N. A. Pertsev, F. Schlaphof, L. M. Eng, C. Ganpule, V. Nagarajan, R. Ramesh, R. Waser, Appl. Phys. Lett., 80, no. 8, 1424-1427, (2002).
- [3] A. Roelofs, T. Schneller, K. Szot, R. Waser, Appl. Phys. Lett. 81, 5231 (2002).

Andreas Roelofs, Kristof Szot

AUTHORS

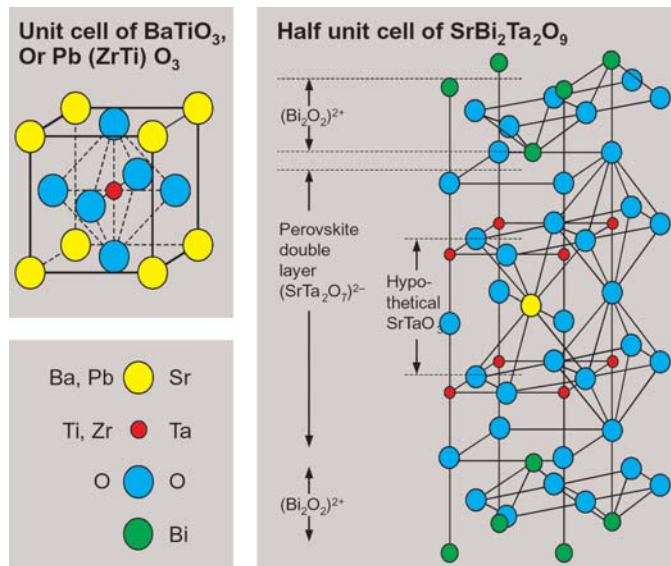
Finite Size Effects in Ultrathin Ferroelectric Films

INTRODUCTION

Dynamic random access memories (DRAMs) are the workhorses for memory chips. They have just one problem: they lose the stored information if the electric power is turned off. Presently the most common nonvolatile memories are "Flash memories" and electronically erasable programmable read only memories (EEPROM). These lack speed, ease and unlimited reprogrammability, and they are expensive. To overcome the drawbacks of Flash and EEPROMs, advanced concepts are explored in order to use either magnetic or ferroelectric materials.

Ferroelectric memories (FeRAMs) use the remanent polarization for non-volatile information storage [1]. In a "standard" dielectric, positive and negative charges are displaced from their original position by the application of an electric field. This creates a dipole moment, the polarization. However, this polarization will vanish, if the electric field returns to zero. In a ferroelectric material, on the other hand, a permanent displacement is inherent to

Fig. 1
Structure of the ferroelectrics
 BaTiO_3 , $\text{PbZr}_{1-x}\text{Ti}_x\text{O}_3$ and the
layered $\text{SrBi}_2\text{Ta}_2\text{O}_9$



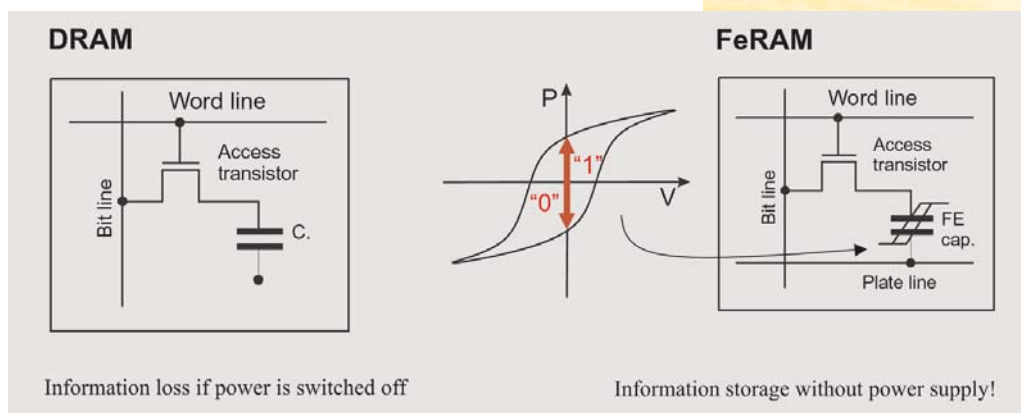
the material and does not disappear in the absence of the electric field. The direction of this polarization can be changed by applying an appropriate field. Fig. 1 shows the unit cells of $\text{PbZr}_x\text{Ti}_{1-x}\text{O}_3$ (a) and $\text{SrBi}_2\text{Ta}_2\text{O}_9$ (b). These materials are the best candidates for the development of FeRAMs.

The fabrication of FeRAMs poses significant technological challenges. In addition, many important details of ferroelectricity are not yet understood. Presently ferroelectric thin films and small particles are considered for dynamic RAM applications. They demand careful studies of the surface effects, influencing the dielectric polarization. Even surface phase transitions have been predicted, but very little is known about ferroelectricity in thin wires, fine particles and ultra-thin films. Part of our research focuses on the investigation of finite size effects in epitaxial ferroelectric films.

Well-defined thin films are crucial for electronic applications of ferroelectrics. The synthesis of these structures by molecular beam epitaxy (MBE), sputtering, and other methods now is yielding devices of high quality and reproducibility. The properties of these systems are strongly influenced by surface and size effects, and by the atomic and electronic structure of the interfaces between the ferroelectric and the metallic electrodes or dielectric layers. Our experiments progress by gradually shrinking the dimensions of the ferroelectric films, while following the changes of the electrical properties. In Fig. 2 the 1 Transistor – 1 Capacitor (1T-1C) cell layout of a DRAM and a FeRAM is shown.

APPROACH

Fig. 2
DRAM and FeRAM cell



Size-effects in ferroelectric thin films

Film Thickness:

historical survey – some milestones

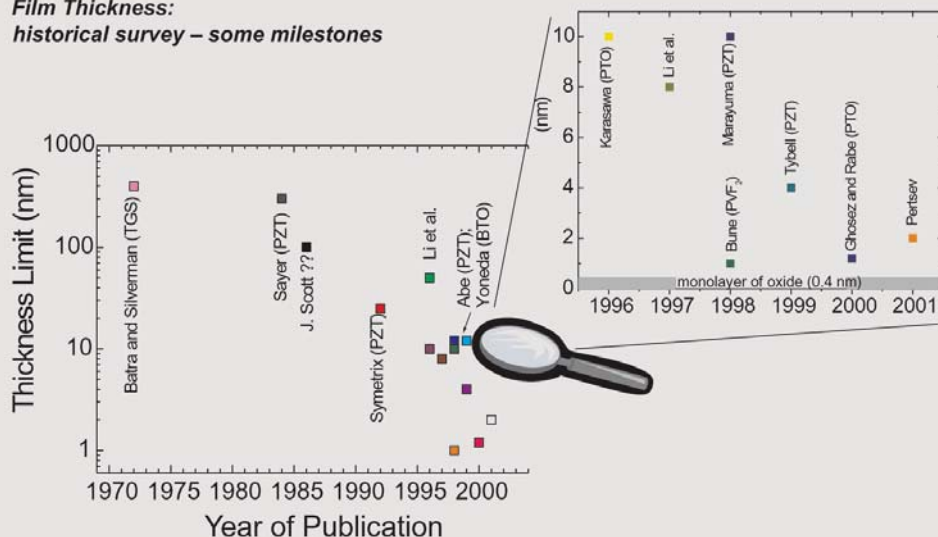


Fig. 3

Decrease of the expected or observed minimum layer thickness of ferroelectrics as a function of the publication year [2]

The polarization vs. voltage hysteresis loop is used to store the bit "0" and "1" in a non-volatile fashion. The thickness of the ferroelectric film is around 100 nm for FeRAMs. A further decrease of the film thickness down to 10 nm and below poses fundamental questions. Eventually the superparaelectric limit will be reached and the ferroelectricity disappears. Ferroelectricity is a cooperative phenomenon like superconductivity and magnetism, where the interaction with an ensemble of unit cells is essential. However, the magnitude of the critical thickness, estimated either theoretically or experimentally, shows a surprising trend: it seems to decrease with time, as shown in Fig. 3. For ferroelectric capacitors using ultrathin films with a thickness of 4 nm or less, quantum mechanical tunneling of electrons through the film during the application of a voltage cannot be ignored anymore [2]. On the other hand, the measurement of tunneling currents may become a powerful tool for studying nanometer-thin ferroelectric films. First results are presented here.

We have prepared single crystalline epitaxial $\text{PbZr}_{0.52}\text{Ti}_{0.48}\text{O}_3$ (PZT) and BaTiO_3 (BTO) thin films on single crystalline epitaxial SrRuO_3 (SRO) films grown on SrTiO_3 (100) (STO) substrates. PZT and SRO films were grown using high-pressure on-axis sputtering and BTO using pulsed laser deposition (PLD). The film thickness ranged from 12 to 165 nm. Their structural properties, surface smoothness and interface quality were demonstrated by X-ray diffraction (XRD), high resolution transmission electron microscopy (HRTEM) and atomic force microscopy (AFM). Rutherford backscattering spectrometry and channeling measurements (RBS/C) were used to analyze stoichiometry and crystalline quality. Ferroelectric hysteresis loops were obtained for all films of a thickness down to 12 nm showing a decrease in the remanent polarization P_r and an increase in the coercive field E_c towards thinner film thicknesses. Examples of some hysteresis loops are shown in Fig. 4 for BTO and PZT. High-resolution transmission electron microscopy (HRTEM) and electron diffraction analysis are employed to characterize the structural properties of the SrRuO_3 / $\text{Pb}(\text{ZrTi})\text{O}_3$ / SrRuO_3 multilayer system [3]. The morphology of the multilayer films along the growth direction and the lattice and defects at the interface area are obtained in cross-sectional lattice images. Fig. 5(a) shows an image recorded with the electron beam parallel to a (100) direction in the film plane. The interfaces between the PZT layer

RESULTS



Fig. 4
Thickness dependence of the hysteresis loops of PZT and BTO

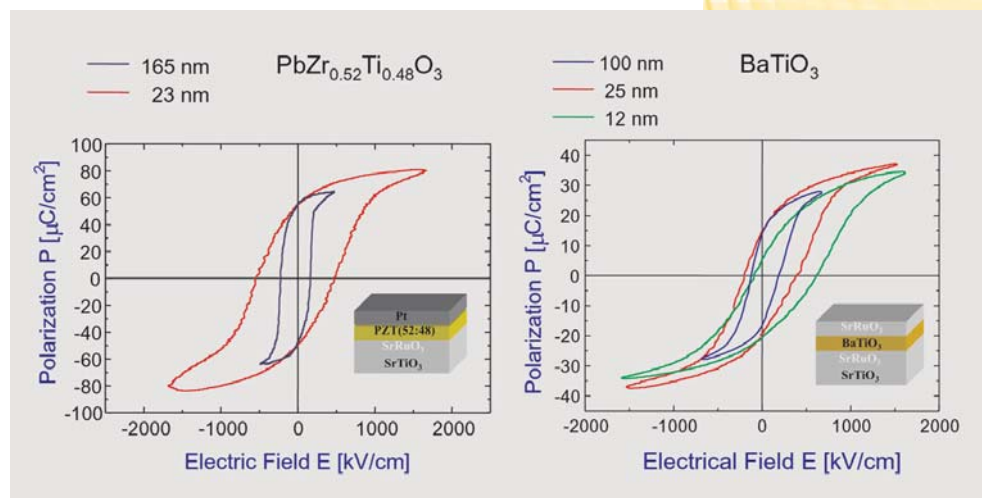
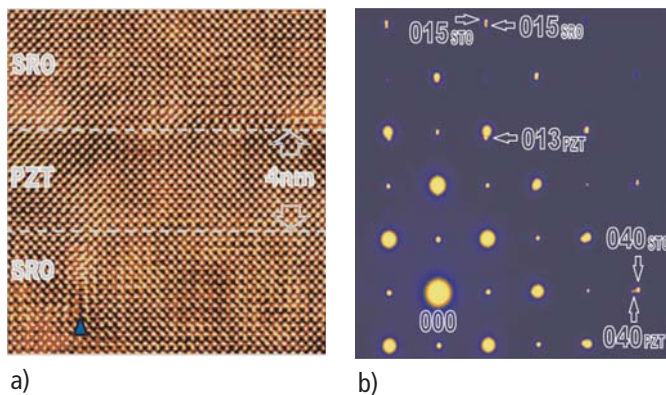


Fig. 5

a) High resolution TEM picture of an epitaxial SRO / PZT / SRO multilayer [3]

b) Electron diffraction pattern of the hetero-structure



and the top and the bottom SRO electrode layers are marked by dashed lines. Along the interface misfit dislocations occur. They allow to relax the stress induced by the lattice mismatch between the two compounds. A dislocation at the lower interface is denoted by a triangle. Analysis of electron diffraction patterns shown in Fig. 5(b) demonstrates that the bottom SRO electrode layer is compressively stressed in the film plane and its in-plane lattice parameter follows that of the STO substrate. The PZT layer shows a lattice parameter very close to that of the bulk and the c-axis is found to be parallel to the film normal. Currently we study even thinner films down to 3 nm. Tunnel junction have been prepared to observe the possible interplay between the ferroelectric polarization reversal and the quantum mechanical tunneling effect.

REFERENCES

1. J. F. Scott, *Ferroelectric Memories*, Series in Adv. Microelectro-nics, Springer- Verlag 2000.
2. H. Kohlstedt, N. A. Pertsev, and R. Waser, *Mat. Res. Symp. Proc. Vol.*,688, 161 (2002).
3. C. L. Jia, J. Rodriguez Contreras, U. Poppe, H. Kohlstedt, R. Waser and K. Urban, *J. Appl. Phys.* 92, 101 (2002).

AUTHORS

Hermann Kohlstedt, Julio Rodriguez-Contreras, Jürgen Schubert, Chunlin Jia

Imprint Effects in Ferroelectric Thin Films for Memories (FeRAMs)

Non-volatile memories are highly desirable for numerous current and future portable applications as high-performance digital cameras, digital audio appliances, mobile phones, PDAs, or Palm PCs. The key parameters of the memory cells are low power consumption, fast write and read times, a number of read and write cycles larger than 10^{15} , compatibility with Si logic devices, and a small cell size for high storage density. Conventional non-volatile memories such as Flash devices only partially fulfill these demands. A Flash memory cell must be erased before rewriting and the number of writing cycles is limited to 10^6 . Also, the writing cycle is rather ineffective because of the time needed. In addition, the power consumption for the writing process exceeds that of other types of RAMs by orders of magnitudes.

A new type of memory device is the ferroelectric random access memory (FeRAM). It incorporates a ferroelectric film at the sub-micron scale as a capacitor to hold data [1], see Fig. 1. The ferroelectric film provides the remanent polarization, which can be reversed by an applied electric field. Most promising candidates of ferroelectric materials are $\text{Pb}(\text{Zr}_{1-x}\text{Ti}_x)\text{O}_3$ (PZT) and $\text{SrBi}_2\text{Ta}_2\text{O}_9$ (SBT). From the material science point of view, the long term stability of the ferroelectric properties has to be guaranteed in order to avoid failures of the memory.

TASK

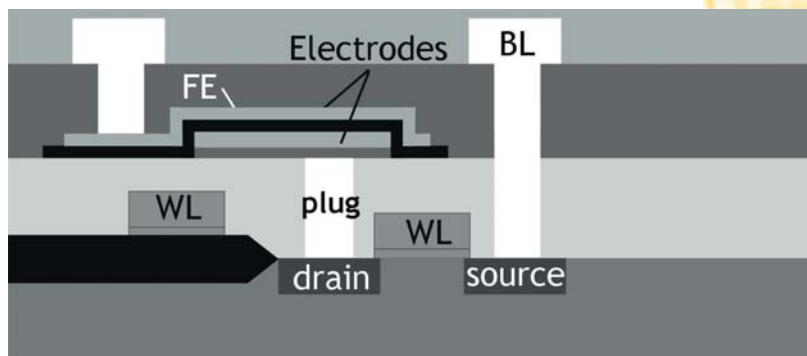


Fig. 1
Schematics of a
stacked FeRAM cell.



Fig. 2

Imprint effects in a ferroelectric capacitor. Switching is no longer possible, because the operation voltage is too low (write failure). No difference between both logic states is detected since the "negative" remanent polarization becomes larger than zero.

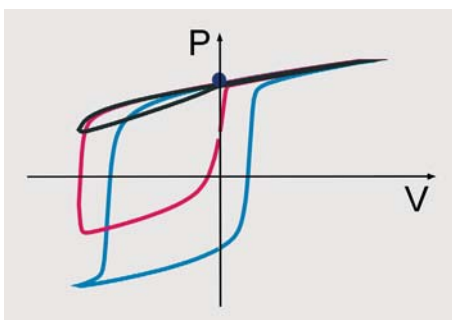
APPROACH

Fig. 3

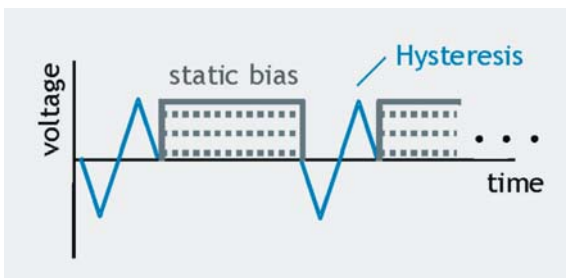
Imprint measurement procedure. The temperature is kept constant for the entire measurement.

Imprint (also called ferroelectric aging) is a critical failure mechanism for ferroelectric thin films used in FeRAMs:

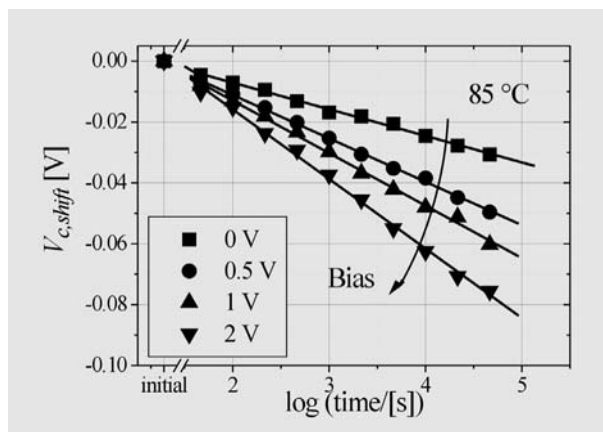
Maintaining a remanent polarization for a long time leads to a shift of the ferroelectric hysteresis loop with respect to the applied voltage (Fig. 2). This process is a function of time. Hence, imprint can cause two ways of failure: Firstly, the memory device becomes non-switchable, if the voltage shift exceeds the writing voltage. Secondly, the sense amplifier may be unable to distinguish between the two different polarization states due to the loss of the remanent polarization caused by the voltage shift. Therefore, a method is required to determine the lifetime of the memory device and the limits caused by the imprint failure.



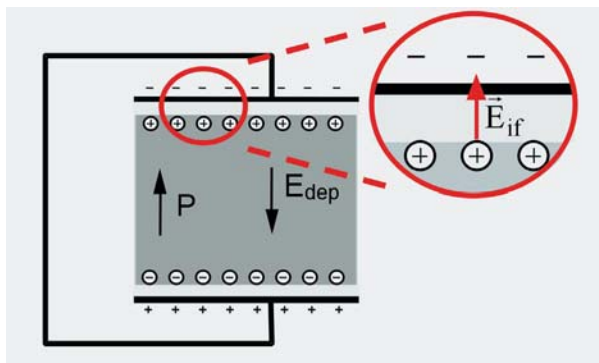
While many investigations about imprint in ferroelectric thin films can be found in the literature, only small efforts had been made to understand the underlying physical mechanisms. Therefore we have conducted detailed studies on the imprint behavior of PZT and SBT, including important parameters such as time, temperature, applied bias, illumination and post anneal processing. The imprint measurement procedure is depicted in Fig. 3. Furthermore, the influence of oxide electrodes on ferroelectric PZT thin films was investigated.



The time dependence of the voltage shift $V_{c,shift}$ follows a logarithmic time dependence, as shown for SBT thin films in Fig. 4. Similar dependencies were found for PZT thin films and BaTiO₃ ceramics [2]. The process is slightly temperature activated with an activation energy of approximately 80 meV. For a given voltage, the shift is independent of the sample thickness (70...120 nm).



Illumination with light of bandgap energy enhances the tendency of ferroelectric thin films to exhibit voltage shifts – indicating that electronic charges play a major role in the imprint scenario. On the other hand, annealing under slightly reducing atmosphere does not affect the imprint behavior – indicating that ionic defects such as oxygen vacancies have a minor influence on the imprint behaviour. Applying a bias in the direction of the polarization during the imprint treatment also enhances the imprint effect of the ferroelectric films.



RESULTS

Fig.4

Time dependence of imprint as a function of the applied field for a ferroelectric SBT thin film capacitor, thickness 190 nm.

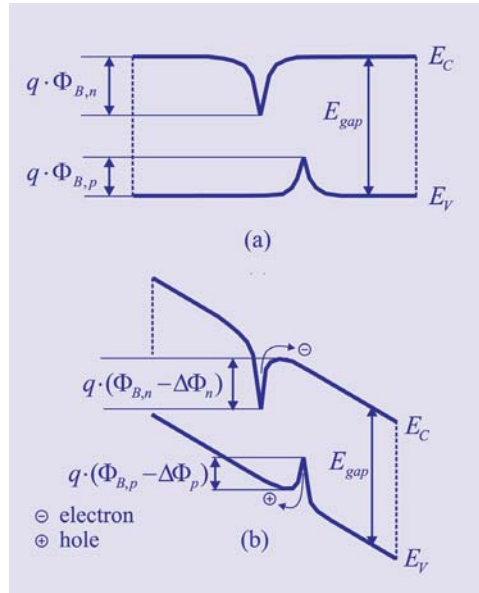
Fig. 5

The electrical field in the dielectric gap at the interface between electrode and thin film E_{if} is responsible for the imprint effect.

Fig. 6

Sketch of the Frenkel-Poole emission of trapped electrons and holes.

- (a) No electric field present in the layer;
 (b) Electric field leads to a barrier lowering by $\Delta\phi_p$ for holes and $\Delta\phi_n$ for electrons.



From these experimental results a model was developed which suggests imprint to be caused by a strong electric field at the interface between the thin film and the electrode [3]. This field arises due to a thin surface layer in which the spontaneous polarization is reduced or even absent – in contrast to the ferroelectric bulk of the films (see Fig. 5). The interface screening mechanism proposed as origin of imprint is presumably caused by a Frenkel-Poole type charge separation within the surface layer, as shown in Fig. 6. The results of numerical simulations support this assumption. For PZT films assuming the polarization to be absent within the surface layer, a good agreement between experiment and simulation is obtained for a surface layer extension of approximately 5 nm (i.e., the sum of both extensions at the top and bottom electrode). In that case the dielectric constant in the surface layer is approximately 30 % lower compared to that of the bulk of the film. In the case of SBT films similar values are obtained.

Fig. 7 shows the comparison of the experimentally observed temperature dependence of imprint with the numerical simulations indicating the existence of shallow traps within the surface layer. The activation energy amounts to approximately 0.3-0.5 eV. The existence of traps within the band gap of the

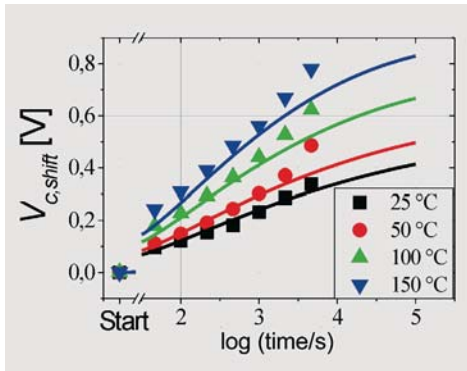


Fig. 7
Experimental data (PZT 30:70, 200 nm, room temperature) and numerical simulation of the voltage shift evolution (line). A good match is obtained for the used set of parameters.

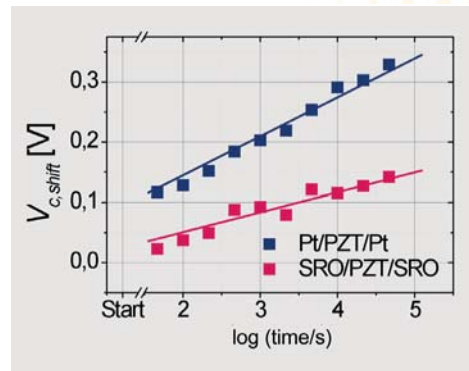


Fig. 8
Imprint behavior of ferroelectric thin films (PZT 30:70, 150 nm, room temperature) with platinum or SrRuO₃ electrodes.

materials under investigation is also confirmed by illumination experiments. Using optical energies smaller than the bandgap of the material, a significant enhancement of the imprint effect is observed - indicating the existence of these traps. The experimental results of the present study can be explained by the proposed model. This includes our results for the dependence of imprint on temperature and on film thickness as well as the improvement of the memory stability and the reduction of the imprint effect by using oxide electrodes (Fig. 8).

- [1] J.F. Scott and C.A. Paz de Araujo, Science 246, 1400 (1989).
- [2] R. Lohkämper, H. Neumann, and G. Arlt, J. Appl. Phys. 68, 4220 (1990).
- [3] M. Grossmann, O.Lohse, D. Bolten, U. Böttger, R. Waser, J. Appl. Phys. 92, 2680 and 2688 (2002).

Michael Grossmann, Ulrich Böttger, Rainer Waser

REFERENCES

AUTHORS



Ferroelectric Thin Films for Integrated Optics

INTRODUCTION

The great importance of ferroelectric thin films for microelectronics, especially new types of nonvolatile memories, is demonstrated in several contributions to this booklet. Another group of contributions describes our progress in the field of **hetero-epitaxy, the epitaxial growth of layers of different materials**. The epitaxy of semiconductor heterostructures is needed for semiconductor lasers, but also for GaN/Si, SiGe/Si, CoSi₂/Si and all the III/V quantum well devices. It is subject to intense research and new developments. The heteroepitaxy of oxides typically is less common and sometimes even more difficult. Nevertheless, the achievements of the high temperature superconducting (HTS) thin film device fabrication, most notably the HTS SQUID sensors, relies on the heteroepitaxy of the superconducting oxide YBa₂Cu₃O₇ on different substrates. Again, many of these issues have been researched in Jülich and a few are communicated in this booklet. **A remaining challenge is the heteroepitaxial growth of optical ferroelectrics in the form of highly transparent thin films**. The optical ferroelectrics are generally grown in bulk form, and it is well known, that impurities, defects and domain structures are scattering centers and impair the optical quality. This makes the epitaxial growth typically more demanding than the deposition of polycrystalline ferroelectrics for electrical applications. The required optical waveguides typically are thin structures, arranged along the surface. Due to the electro-optical properties, they can form active elements as modulators or switches. We have grown single domain optical ferroelectric layers and patterned them into integrated optical devices.

APPROACH

Presently our work is focussed on the epitaxy of transparent ferroelectric BaTiO₃, grown on (100) MgO substrates. For the growth process, we use the pulsed laser deposition (PLD), typically with a laser power of 1100 mJ/pulse and a substrate temperature of 800°C, while maintaining an oxygen pressure of

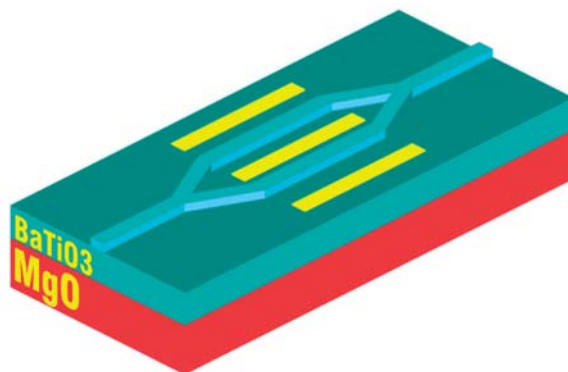


Fig. 1
Schematic of a Mach-Zehnder waveguide modulator. Typical dimensions: length 9 mm, width 50 μm , waveguide ridge 50 nm high. The Au electrodes (3 mm x 5 μm) are denoted by yellow stripes.

10^{-3} mbar within the chamber [1]. The deposited BaTiO_3 films form planar optical waveguides, because they are grown on a substrate with a lower index of refraction. They are highly transparent, permitting optical guiding across the device with losses of less than 3 dB/cm. The ridge type waveguides are 50 nm high and 2000 nm wide. These waveguides are monomode for wavelengths of 633 to 1500 nm. They have been patterned by lithography and ion beam etching into the form of Mach-Zehnder (MZ) modulators, see Fig. 1. The length of the electrodes is 3 mm and the distance between adjacent electrodes 10 μm . Each substrate is 10 x 10 mm in size and offers enough space for an array of 50 MZ devices. A view of 13 devices through the microscope is shown in Fig. 2. Only the Au electrodes and the tips of two contact needles are visible, the waveguides themselves are transparent. The set-up for the electro-optic measurements is

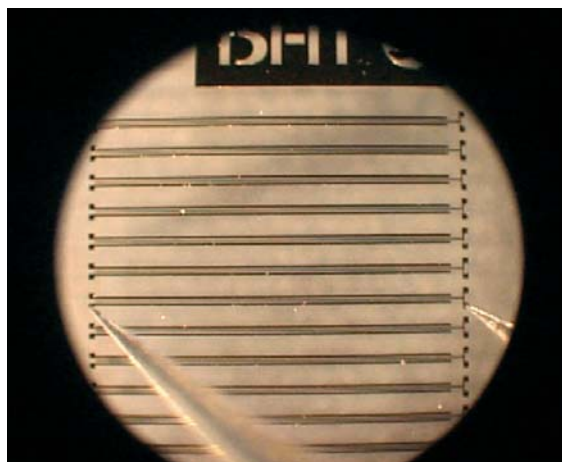
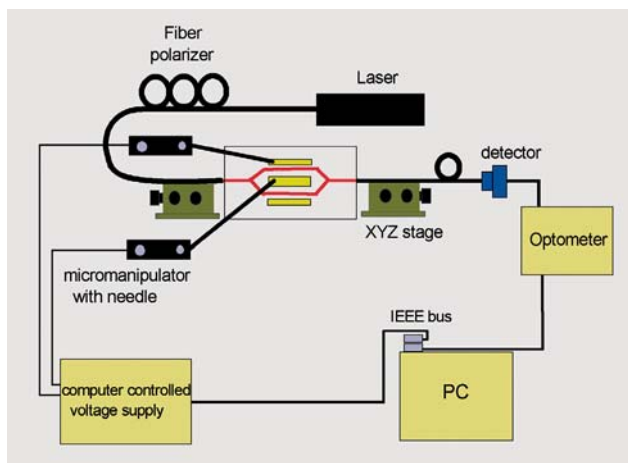


Fig. 2
A view through the microscope, showing the arrangement of the Au electrodes and two contact needles. The waveguides themselves are transparent.

Fig. 3
Schematic of the setup for
measurements of the elec-
trooptic properties



shown in Fig. 3. The output of a laser is coupled into a single mode fiber. A fiber polarizer is used to define the input polarization. The modulators themselves are polarization maintaining. The light is „endfire“ - coupled into the MZ array. Contact needles are used to apply the voltage to the middle and to one outer electrode. The output is coupled to a photo detector and the transmitted optical intensity is measured as a function of the applied voltage.

RESULTS

Experimental results are shown in Fig. 4. The form of the observed modulation curves is exactly as predicted by theory [2]. For films with the *c*-axis perpendicular to the substrate, the numerical values of $n_o = 2.349$ and $n_e = 2.324$ for the ordinary and extraordinary refractive indices at 633 nm have been determined. At the same wavelength, a modulation voltage of $V_\pi = 8$ V was measured, leading to a Pockels coefficient $r_{51} = 80$ pV/m. If the conditions during PLD deposition are modified, the films can be grown with the *c*-axis oriented in plane. In this case, an effective electrooptic coefficient of 54 pm/V leads to an even stronger optical modulation ($V_\pi = 6.3$ V). The frequency response of these devices was measured up to 1 MHz and did not show any degradation. Measurements at higher frequencies are in preparation.

The low V_π values and the short length of the electrodes (3 mm) make these devices very attractive for the integration into

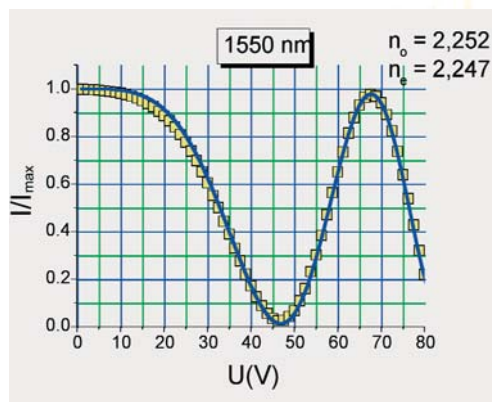
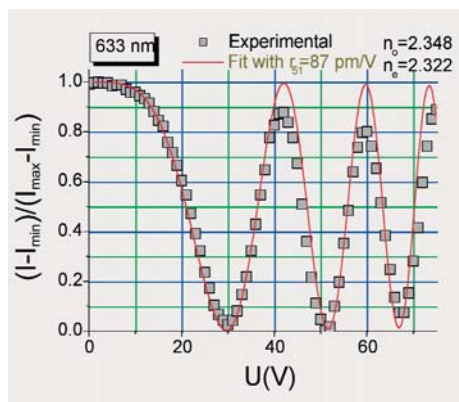


Fig. 4
Intensity modulation of a c-axis MZ modulator vs. applied voltage at 633 nm (left) and 1550 nm (right). The lines are the result of modelling calculations.

microelectronic circuits. Our future experiments will study the epitaxial growth on different substrates, especially on oxide buffer layers, which are deposited onto silicon wafers. First experiments indicate, that a lower growth temperature still may lead to useful electrooptical properties. This is very important, because silicon and oxides typically have different thermal expansion coefficients and the thermal stress and strain during cooling from the high growth temperatures may degrade the films.

1. Structural and optical characterization of epitaxial waveguiding BaTiO₃ on MgO
L.Beckers, J.Schubert, W.Zander, J.Ziesmann, A.Eckau, P.Leinenbach, Ch.Buchal
J. Appl. Phys. 83 (1998) 3305
2. Ferroelectric BaTiO₃ thin-film optical waveguide modulators
A.Petraru, J.Schubert, M.Schmid, Ch. Buchal,
Appl. Phys. Lett. 81 (2002) 1375

Adrian Petraru, Jürgen Schubert, Christoph Buchal

REFERENCES

AUTHORS



Novel Dielectric Structures for Advanced High Frequency Communication and Sensor Systems

INTRODUCTION

Dielectrics play an important role for advanced microwave communication systems. For example, dielectric resonators composed of ceramic cylinders are of common use for filters in satellite and mobile communication systems. Novel dielectric structures will help to fulfil the demands for future millimetre and sub-millimetre wave communication and sensor applications, namely improved performance by advanced electromagnetic designs and by operation at cryogenic temperatures, diversified functionality by on-chip **integration of nonlinear dielectric and metallic nanostructures and the exploitation of the millimetre wave regime up to Terahertz frequencies** by electromagnetic bandgap structures aiming toward a novel integrated millimetre wave technology. As an example, in mobile communication an increase of device performance is essential in order to utilise the available narrow frequency bandwidth most efficiently. On the other hand, on-chip integration is an important issue addressing the enormous cost pressure in the wireless communication industry. Sensor applications based on millimetre waves ranging from collision avoidance radar systems for automobiles and imaging systems for airport security inspection to possible biomedical applications are still in their infant state. Novel dielectric structures in conjunction with the strongly progressing efforts in the field of active semiconducting devices for millimetre waves may pave the way to such new applications.

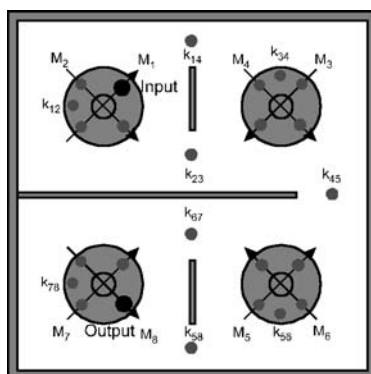
APPROACH

We combine our expertise in the field of preparation and investigation of functional materials with the design of novel devices and advanced high frequency characterisation techniques. The available methods are metal and oxide multilayer deposition

techniques in conjunction with patterning techniques including electron beam lithography as well as advanced machining of bulk ceramics. Our electromagnetic simulation capabilities are essential for designing novel high-frequency devices and circuits. In addition, high-frequency characterisation techniques like network analysis, phase noise and intermodulation measurement capability including systems for millimetre wave characterisation represent the basic requirement for advanced material and device characterisation.

Dielectric filters for communication base stations and satellites

We have developed a novel type of dielectric filter based on an advanced inter-resonator coupling scheme being applicable for cylindrically or hemispherically shaped bulk dielectric resonators. Fig. 1 shows an example of an eight-pole filter composed of four dielectric resonators (large circles) being mutually coupled by metallic apertures (gaps in the metal housing equipped with dielectric tuning screws). The 45 degree orientation of the dual-mode polarisation resulting from the angular position of the tuning screws (small grey circles) and input and output coupling antennae (small black circles) results in negative coupling $k_{i,j}$ coefficient between non-adjacent resonances ($i \neq j \pm 1$). Negative coupling generates damping poles in the filter characteristic which can be utilised to build filters with an extremely steep filter response function at the edges of the passband. Our novel dielectric filter allows for higher Q values, i.e. lower transmission losses within the passband of the filter characteristic. In particular, when cooled to cryogenic temperatures, a power loss of less than - 0.1 dB (2.3 %) has been demonstrated.



RESULTS

Fig. 1:
Novel type of dielectric filter composed of an advanced inter-resonator coupling scheme. This scheme allows the realisation of an elliptic filter type response curve with low in-band insertion loss. The small circles labelled by k_{ij} correspond to dielectric tuning screws to adjust the coupling between modes M_i and M_j .

Fig. 2:
Prototype of a 3-channel
cryogenic output multiplexer
for satellite communication
built at Bosch SatCom GmbH
(now: Tesat GmbH) based
on the dielectric filter
concept developed at FZJ.

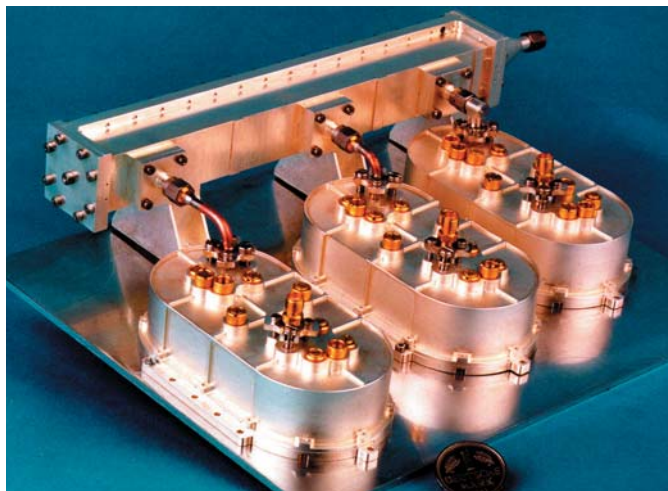


Fig. 2 shows a prototype of a 3-channel cryogenic output multiplexer for satellite communication built at Bosch SatCom GmbH, being composed of three 4-pole filters based on our dielectric filter concept. This prototype was planned for a cryogenic satellite system demonstration experiment on the International Space Station (ISS).

Cryogenic oscillators with low phase noise

The quantity "phase noise" describing frequency fluctuations of the output signal of a microwave oscillator represents an important figure-of-merit, which limits the sensitivity of a radar system and the maximum data rate of a communication link. Typically, an oscillator is composed of an integrated semiconductor low-noise microwave amplifier arranged in feedback operation with a high-Q microwave resonator with its resonant frequency set at the desired frequency. Usually, oscillator phase noise results from charge carrier fluctuations in the transistor, typically high-electron mobility transistors, so-called HEMTs, based on GaAs or InP.

Resonators with extremely high Qs, i.e. with extremely narrow resonance curves, represent an approach to minimise the oscillator phase noise. We have developed so-called "whispering-gallery (WG) mode resonators", each composed of a disc of high-purity sapphire being assembled in a metallic housing.

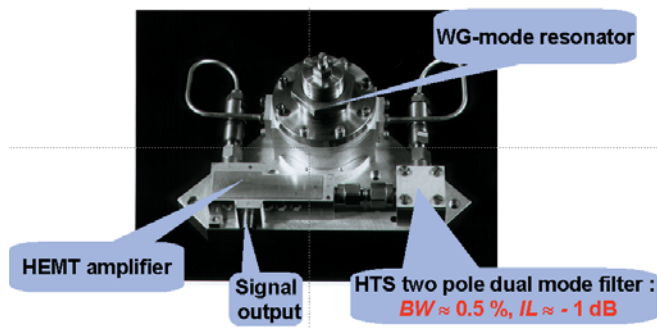


Fig. 3

Photograph of our cryogenic low-phase noise oscillator assembly composed of a sapphire whispering gallery (WG) resonator, a semiconducting HEMT amplifier and a high-temperature superconducting (HTS) mode selection filter.

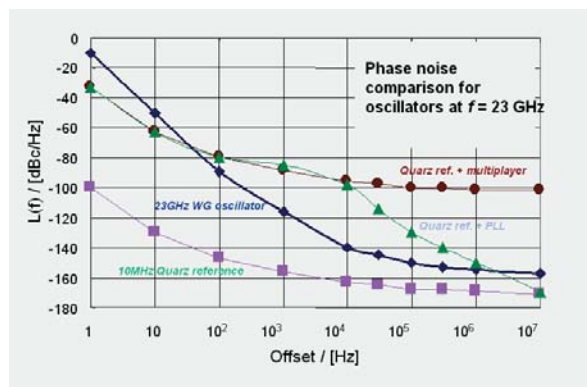


Fig. 4:

Measured oscillator phase noise as a function of frequency offset from the carrier frequency at 23 GHz for our cryogenic oscillator (blue) in comparison to conventional low-phase noise oscillators at 23 GHz (brown and green) based on a 10 MHz quartz reference (pink) .

Due to strong confinement of the electromagnetic field energy caused by internal total reflection, the Qs are only depending on the dielectric losses in the sapphire disc, which are extremely low at cryogenic temperatures. Fig. 3 shows our WG resonator connected with a low-noise amplifier being assembled on a small cryogenic platform. At an operation temperature of 77 K, the Q of our resonator operating at 23 GHz exceeds one million, which results in an oscillator phase noise being lower than that observed for any other technique (Fig. 4).

Thin film dielectric nanostructures for tuneable microwave circuits

Oxide perovskites like $\text{Ba}_x\text{Sr}_{1-x}\text{TiO}_3$ exhibit a strong electric field dependence of the dielectric constant which can be utilised for the construction of voltage controlled capacitors (varactors) for microwave integrated circuits.



Fig. 5
Electron micrograph and schematic view (insert) of a vertical varactor structure consisting of a SrTiO_3 ridge of $2\ \mu\text{m}$ width and copper electrodes.

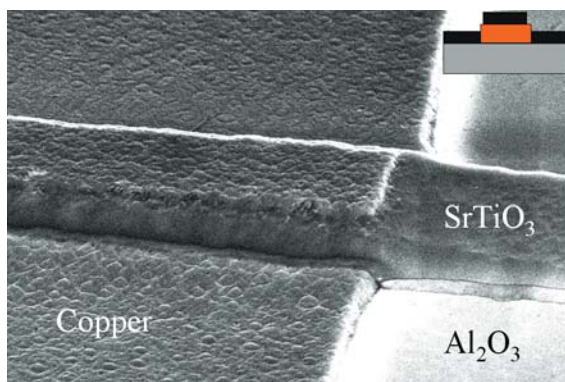


Fig. 6
Comparison of the tuneability as a function of bias voltages of our vertical capacitors in comparison to conventional planar capacitors.

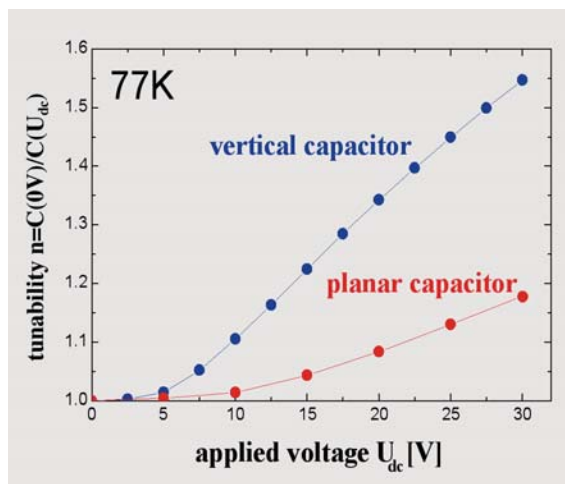


Fig. 6 shows the measured tuneability (normalised capacity at a given bias voltage) as a function of bias voltage. In contrast to conventional planar capacitors, our vertical capacitors as shown in Fig. 5 exhibit a large tuneability at relatively low bias voltages. Moreover, our varactors exhibit quite low dielectric losses at microwave frequencies, which is essential for future integrated micro-and millimetre wave circuits.

Electromagnetic bandgap structures for millimetre waves

“Electromagnetic bandgap (EBG) structures” or “photonic crystals” are two- or three dimensional periodic arrangements of dielectric materials. Similar to the electronic bandgaps of a real crystal, EBG structures exhibit frequency intervals where the propagation of electromagnetic waves is forbidden (electromagnetic bandgaps). Within such bandgaps, waves excited from the surface of an EBG structures or from defects inside the EBG structure decay exponentially on the length scale of a few lattice periods. We use different types of lattice defects for guiding and storing electromagnetic energy, aiming towards novel integrated circuits for the millimetre wave frequency range (about 30 GHz to a few Terahertz).

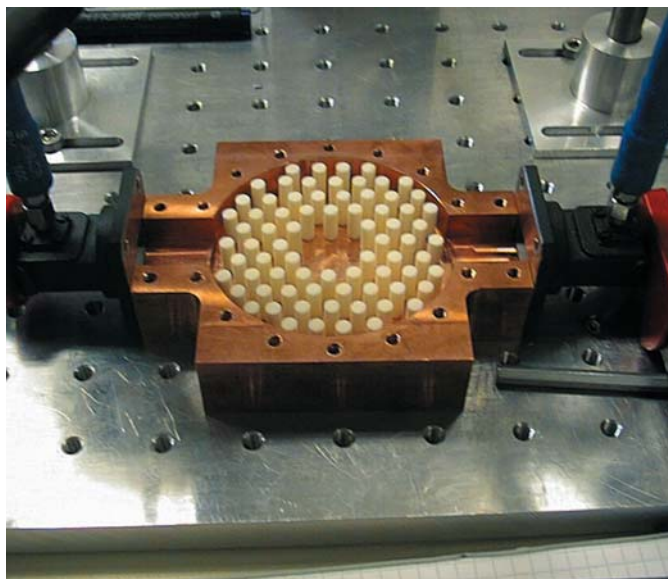


Fig. 7
Alumina rod assembly for test measurements on electromagnetic bandgap defect structures at microwave frequencies.

Fig. 8

Measured frequency dependence of the transmission coefficient of the EBG structure shown in Fig. 7 indicating the effect of the energy gap and two distinct peak corresponding to defect resonances.

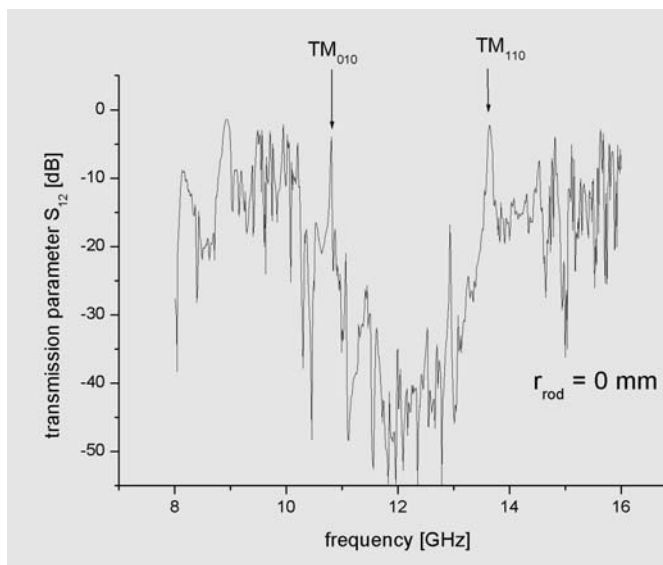


Fig. 7 shows a microwave test assembly for the investigation of defects in a 2D lattice of dielectric rods arranged inside a metallic cavity. The particular defect shown here is an extended point defect generated by omitting seven alumina rods from the central region of the EBG lattice.

The measured frequency dependence of the transmission coefficient (Fig. 8) between the two oppositely faced standardised waveguide ports being matched to the EBG defect structure exhibits a broad frequency interval with reduced transmission caused by the bandgap and two sharp peaks of high transmission within the bandgap. According to our simulations depicted in Fig. 9, these peaks correspond to defect resonances with the electromagnetic field energy being concentrated within the defect region.

Our current efforts are concentrated on the preparation of integrated ceramics EBG structures employing a ceramic moulding technique based on micropatterned polymer moulds.

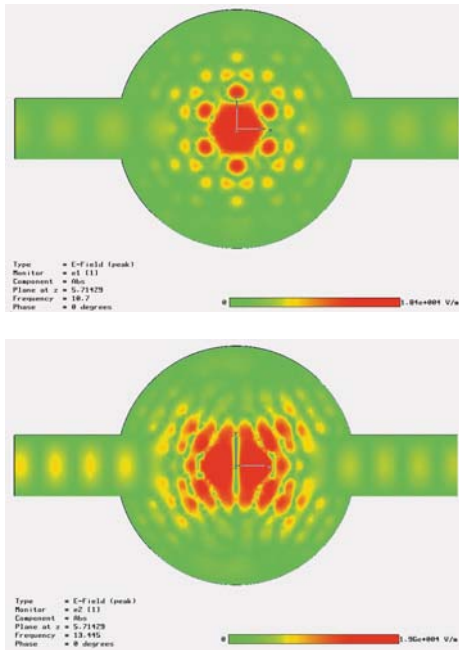


Fig. 9
Calculated distribution of the electromagnetic field amplitude at the frequencies of the peaks apparent in Fig. 8 indicating defect resonances with different symmetry with electromagnetic field energy confined in the region of the defect area.

“Improved designs of tunable ferroelectric capacities for microwave applications”

R. Ott and R. Wördenweber, Appl. Phys. Lett. 80 (2002) 2150.

“Design and characterization of an all-cryogenic low-phase noise sapphire K-band oscillator for satellite communication”

S. Vitusevich, K. Schieber, Indra. S. Ghosh, N. Klein, M. Spinnler
IEEE Transactions on Microwave Theory and Techniques,
January 2003.


“Superconductors and Cryogenics for Future Communication Systems”

M. Klauda, T. Kässer, B. Mayer, C. Neumann, F. Schnell, B. Aminov,
A. Baumfalk, H. Chaloupka, S. Kolesov, H. Piel, N. Klein, S.
Schornstein, M. Bareiss, IEEE Transactions on Microwave Theory
and Techniques 48 (2000) 1227.

**Roland Ott, Michael Schuster, Svetlana Vitusevich,
Roger Wördenweber, Norbert Klein**

REFERENCES

AUTHORS



High-Temperature Superconductor Josephson Multijunction Circuits for Quantum Metrology and Precision Measurements

INTRODUCTION

One of the most attractive applications of the Josephson effect in superconducting electronics is connected with the development of quantum voltage standards. The principal importance of this application is based on the fact that other physical effects are not known today, which could provide a similar accurate representation of the volt. The base of the present voltage standards constitute series of arrays of Josephson junctions. Recently it was shown that a precision digital-to-analogue converter with quantum-mechanical accuracy may be developed on the base of such circuits. A new device will find the following applications:

- as an ac and dc voltage standard as well as a novel Johnson noise temperature standard;
- as an arbitrary precision waveform synthesizer with a record low phase noise;
- as a low harmonics distortion signal source for communication systems and low-noise radar.

Usually niobium junctions working at helium temperatures are applied in such systems. In Jülich a reproducible technology of high-temperature superconductor (HTS) Josephson junctions working at liquid nitrogen temperatures has been developed.

APPROACH

HTS Josephson junctions can be utilized in quantum metrology. The main advantage of HTS is the higher operation temperature, which can be provided by low-power cryocoolers. However, in comparison to niobium Josephson junctions the parameter spread of HTS junctions is relatively high. We developed bicrystal arrays with external shunt resistors (Fig. 1a). Shunted bicrystal

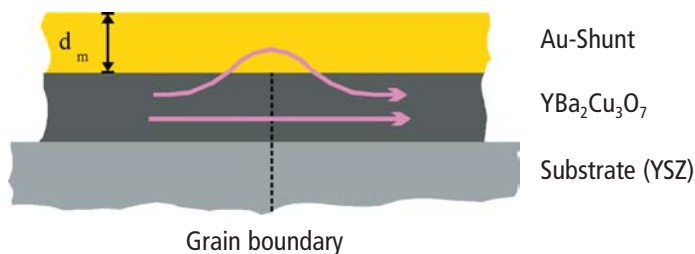


Fig. 1 (a)
Schematic view of the
shunted bicrystal junction.

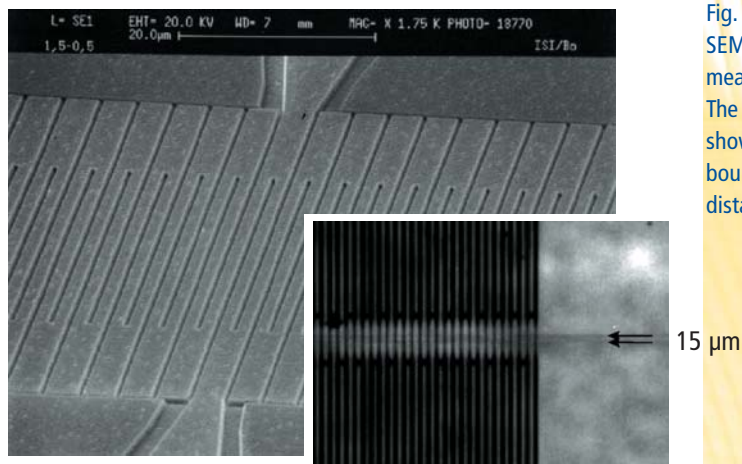


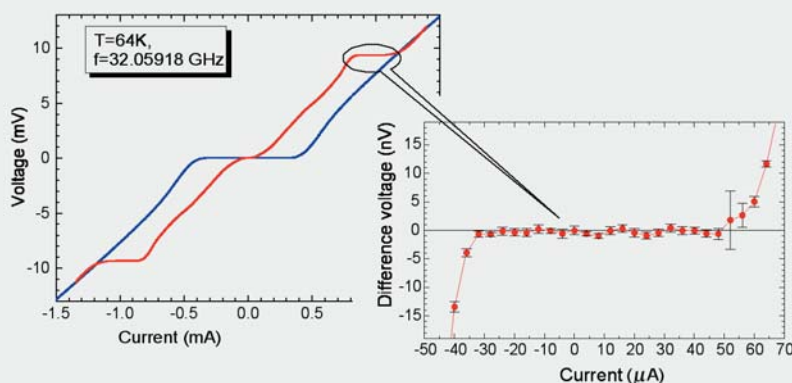
Fig. 1 (b)
SEM micrograph of the
meander series array.
The arrows in the insert
show two parallel grain
boundaries with 15 mm
distance.

junctions were fabricated using Au-YBa₂Cu₃O₇ bilayers deposited in situ on symmetrical yttrium-stabilized zirconium oxide (YSZ) substrates with a misorientation angle of 24°. The meander-like sub-mm structure (Fig. 1b) was fabricated by electron beam lithography and etching. With such an array the variation of the junction's normal state resistance R_n is reduced to a few percent only, whereas the critical current I_c is still varies up to 50 %. Under these conditions, the individual voltage steps of all N junctions emerge within an overlapping current interval. This leads to one single voltage step of reasonable width (with respect to thermal noise) for the whole array at a voltage $U = N f/K_J$, where f is the irradiation frequency and $K_J \equiv h/2e$ the Josephson constant.

RESULTS **Accurate measurements of quantum voltage steps on arrays of Josephson junctions**

Quantum voltages of an array of 136 $\text{YBa}_2\text{Cu}_3\text{O}_7$ bicrystal junctions were calibrated against a programmable niobium based Josephson voltage standard at Physikalisch-Technische Bundesanstalt in Braunschweig. We demonstrated that steps of the current-voltage characteristics of an array of bicrystal junctions at voltages $U \approx 10$ mV were flat to within 6 parts in 10^8 (Fig. 2). The coincidence of quantum voltages on the array of high-temperature superconductor junctions at 64 K and the reference voltage on the array of niobium junctions at 4.2 K was measured with an uncertainty of 1.8 parts in 10^8 . With the same uncertainty, the coincidence of the Josephson constant in $\text{YBa}_2\text{Cu}_3\text{O}_7$ and in metallic superconductors was revealed. Due to this result, HTS arrays are now considered to be very promising with respect to their potential use in high precision voltmeters or secondary standards without the necessity of calibration against a primary standard. If a much larger number of junctions can be realized, HTS could provide the primary standards. The maximum number of synchronized HTS junctions is 431 with an output reference quantum voltage of 20 mV. Current research activities are associated with the development of improved schemes for uniform microwave irradiation for a larger number of integrated junctions.

Fig. 2
Series array of 136 bicrystal junctions (a) without and (b) with microwave power at frequency $f = 32.06$ GHz. Insert shows high resolution plot of the first quantum voltage step.



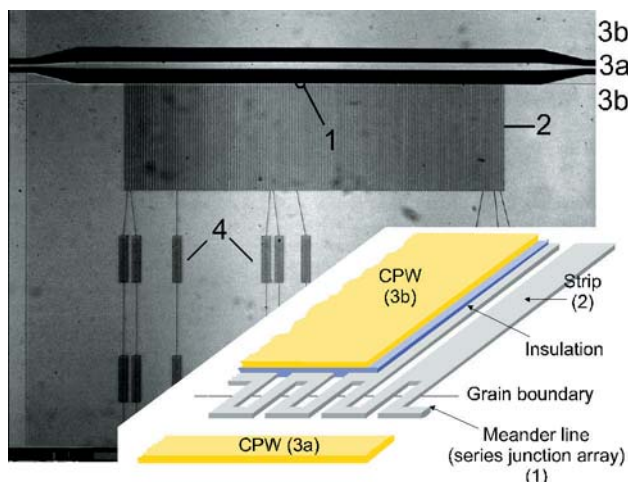


Fig. 3
Integrated microwave
circuit for digital-to-analog
converter.

Microwave circuit for a programmable voltage standard

A laboratory prototype of a microwave circuit for a programmable voltage standard containing 256 shunted bicrystal junctions was designed and studied (Fig. 3). The series array follows a meander line, which limits the uniform distribution of microwave power along the array. In an improved design we place the meander parallel to a coplanar waveguide line. This provides parallel feeding of microwave power to the series connected junctions. A circuit divided in 8 sub-arrays represents a seven-bit digital-to-analogue converter. At a frequency of 27332 MHz and for constant power each of the segments of the array demonstrated the first current step at 78 K (Fig. 4).

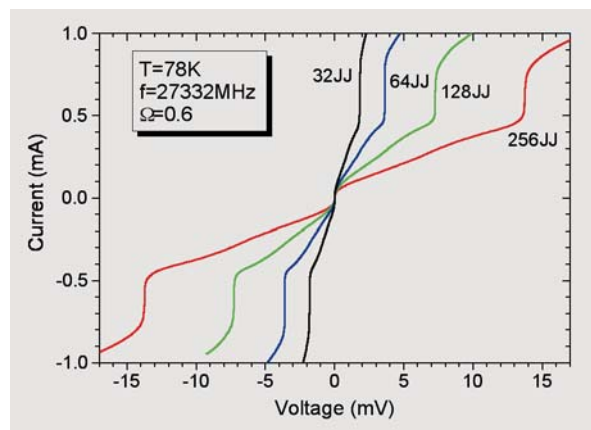
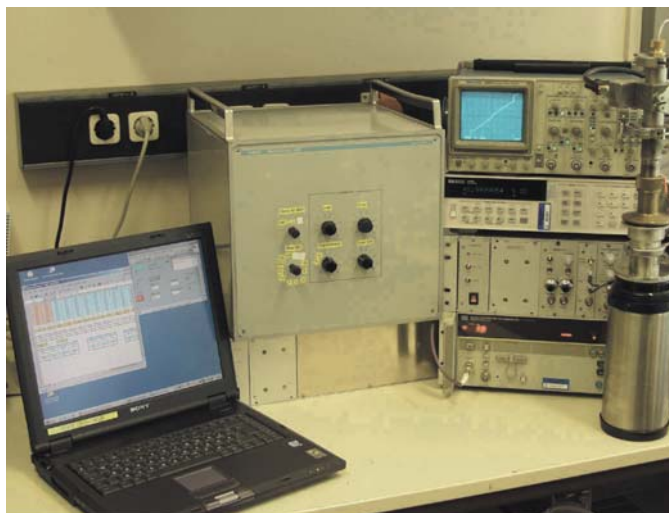
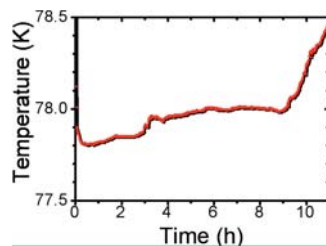
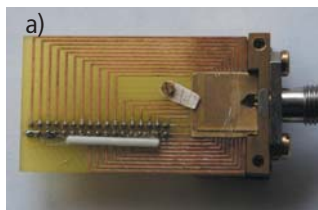


Fig. 4
Simultaneous I-V curves for
three segments and full array
of 256 junctions.

Fig. 5

a) Array of 256 HTS Josephson junctions embedded in a coplanar slot line.

b) Laboratory prototype of the voltage calibrator. Operation time of 1.5 l thermos with liquid nitrogen is approximately 8 hour.



b)

Josephson voltage calibrator

Voltage references used in secondary voltage standards, voltage calibrators and digital volt-meters are based on Zener diodes. The specified stability over a one-year period of the 10 V output of the Zener standard is of the order of one part in 10^6 of the nominal output voltage. Upon properly accounting for temporal drift, pressure, temperature and humidity effects, un-certainties of the order of a few parts in 10^8 over periods of months have been claimed. But this uncertainty can be expected for single instruments with individually measured characteristics only. The Josephson reference voltage based on arrays of HTS junctions permits to retain the small uncertainty of the secondary voltage standard over the whole operating period.

We have developed a laboratory prototype of a voltage calibrator, in which a Zener reference voltage can be calibrated against a quantum voltage generated by an HTS array of Josephson junctions (Fig. 5). Stable voltages up to 10 V in steps of 0.1 V can be obtained with an uncertainty equal to a few parts in 10^8 . Moreover reference voltages from 0.1 V to 10 V in steps of 0.1 V can be obtained and used for testing the linearity of precision digital voltmeters with the same low uncertainty. A link between the Josephson standard and the Zener reference permits to measure the influence of pressure, temperature and humidity on the output voltage of the electronic standard. Also, it helps to overcome the problem of the deviation of the Zener voltage from the linear drift model, which significantly contributes to the uncertainty.

Accurate Measurements of Quantum Voltage Steps on Arrays of Bicrystal Josephson Junctions

A. M. Klushin, R. Behr, K. Numssen, M. Siegel and J. Niemeyer
Appl. Phys. Lett., v. 80, N. 11, pp. 1972-1974, 2002.

A. M. Klushin, Schaltanordnung für Spannungsnormale,
Patent DE 198 06 907 C2, (2002).

DC voltage calibrator based on an arrays of high-temperature superconductor Josephson junctions,

A. M. Klushin, A. V. Komkov, V. D. Gelikonova, S. I. Borovitskii, M. Siegel

IEEE Trans. Meas., to be published 2003.

Alexander Klushin, Norbert Klein

REFERENCES

AUTHORS

High- T_c Superconducting Magnetometers with Submicrometer Bicrystal Junctions for Information Technology

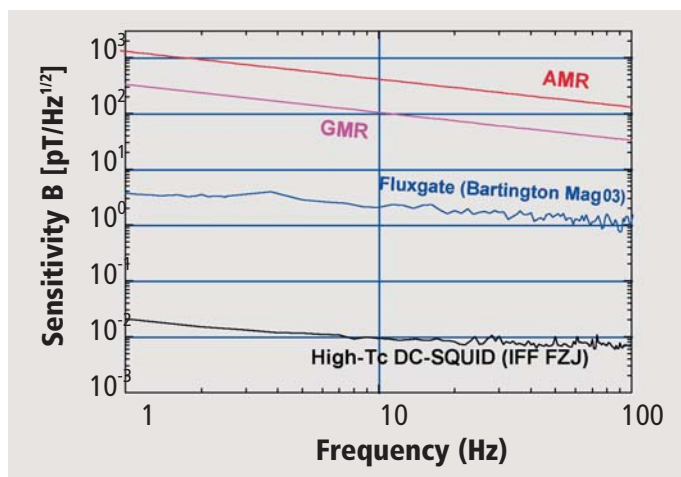
INTRODUCTION

Superconducting **QU**antum **I**nterference **D**evice (SQUID) magnetometers permit the ultimate combined field and spatial resolution. Unsurpassed magnetic field sensitivity (see Fig. 1) and wide bandwidth of the SQUID sensors allows a large variety of measurement systems with unique resolution for different applications in non-destructive evaluation, as testing materials and integrated circuits, or in biomagnetism (magnetocardiography, magnetoencephalography, and the propagation of signals in neurone networks).

The high- T_c SQUID sensors, developed and produced in the Institut für Festkörperforschung (IFF) and distributed by the Technologie-Transfer-Büro (TTB), show the world best sensitivity at the moment [1] and have already found many applications in scientific laboratories around the world. A non-contact evaluation of semiconductors using a laser SQUID microscope was performed in Japan with such SQUIDs. Another example of a SQUID

Fig.1

Comparison of the sensitivities of the high- T_c SQUIDs with conventional magnetometers.



measurement system is a SQUID microscope, which can be used in failure analysis, yield, reliability, and design verification to identify critical defects in high density multilayer printed boards, multilayer structures for magnetoelectronics, Multi-Chip Module (MCM) substrates, in semiconductor packages, wafers, and processes.

The need to further improve the parameters of high- T_c SQUIDs has determined the present trend of reducing the width of the used Josephson junctions to a submicrometer scale [2]. To obtain the best field sensitivity of the SQUID sensors multiturn flux transformers are necessary, requiring a high quality multilayer high- T_c technology. Different SQUID microscope systems incorporating the developed SQUID sensors were found to be adequate for many information technology applications.

Submicrometer bicrystal junctions

The present 24° bicrystal Josephson junctions (see Fig. 2) have a width between $0.4\ \mu\text{m}$ and $1\ \mu\text{m}$, and a critical current density of about $2 \times 10^4\ \text{A}/\text{cm}^2$ at $77.4\ \text{K}$. The junctions are prepared by conventional photolithography and an Ar ion milling process. Some inclusions of secondary phases serve as effective flux pinning centers in the high- T_c films.

It is important to achieve the highest possible microstructural quality of the high- T_c films and Josephson junctions. The average size of the growth spirals of the $\text{YBa}_2\text{Cu}_3\text{O}_{7-x}$ films, deposited by the high-oxygen-pressure dc-sputtering technique, is about $1\ \mu\text{m}$ compared to the about $0.3\ \mu\text{m}$ grains of conventional laser-ablated films. By preparation of submicrometer Josephson junctions with sputtered films one can produce the junctions between individual growth spirals. This improves the homogeneity and increases the tunneling part of the critical current density of the Josephson junctions.

APPROACH

RESULTS

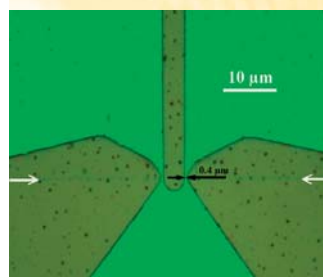


Fig.2
Optical image of the bi-crystal junctions, obtained in a combination of transmission and reflective illumination. A magnification of $\times 1000$ and a green filter were used. The white arrows indicate the position of the bicrystal boundary. The black arrows determine the width of the $0.4\ \mu\text{m}$ wide junction.

Multilayer high- T_c technology

The investigation of epitaxial heterostructures, as multilayer Josephson junctions, crossovers, and vias, helps to obtain the best field resolution of the sensors. Multilayer flux transformers are prepared by a technique developed in IFF using a $\text{PrBa}_2\text{Cu}_3\text{O}_{7-x}$ insulation layer between the windings of the multiturn input coil and the return strip. PMMA-photoresist and Br-ethanol chemical etching are used for surface-damage-free patterning of bottom layers. The $\text{PrBa}_2\text{Cu}_3\text{O}_{7-x}$ film prevents a superconducting short-age and provides a normal conducting shunt of the multilayer flux transformer to attenuate high-frequency resonances in the multiturn coil structure.

The dynamic range of the sensors is mainly limited by the critical current of the flux transformer. Due to the damage-free interfaces and gently sloping edges produced by the Br-ethanol etching we have achieved a critical current for the transformer inner coil of about 100 mA at 77.4 K. For a 8 mm magnetometer (see Fig.3) the pick-up loop has an inductance ~ 20 nH. The dynamic range of the magnetometer limited by the critical current of the flux transformer is about 60 μT (peak-to-peak). This allows sensitive measurements with the magnetometers even after a movement in the earth's field. The development and optimization of HTS structures is very effective by incorporating them in a biomagnetic measurement system, because it requires an ultimate combination of field- and spatial resolution achievable exclusively with SQUID sensors. Test magnetocardiograms (MCG) were measured under clinical conditions with a volunteer having reduced peak-to-peak amplitude of the magnetic signal of heart. The obtained field resolution of about $6 \text{ fT}/\sqrt{\text{Hz}}$ (77K) is similar to the resolution of a standard low- T_c system. But the high- T_c system has at least an advantage of a more than 5 times longer cryogen hold time due to the use of liquid nitrogen instead of liquid helium.

The flip-chip magnetometers are sealed vacuum-tight in fiber-glass epoxy encapsulations, which ensure the long-term stability of the sensors.



Fig. 3
Multilayer flux transformer on 10 mm x 10 mm SrTiO_3 substrate and encapsulated dc-SQUID magnetometers. The magnetometers are fixed on standard dc-SQUID packages (axial and 90°) designed for operation together with iMAG electronics (Tristan).

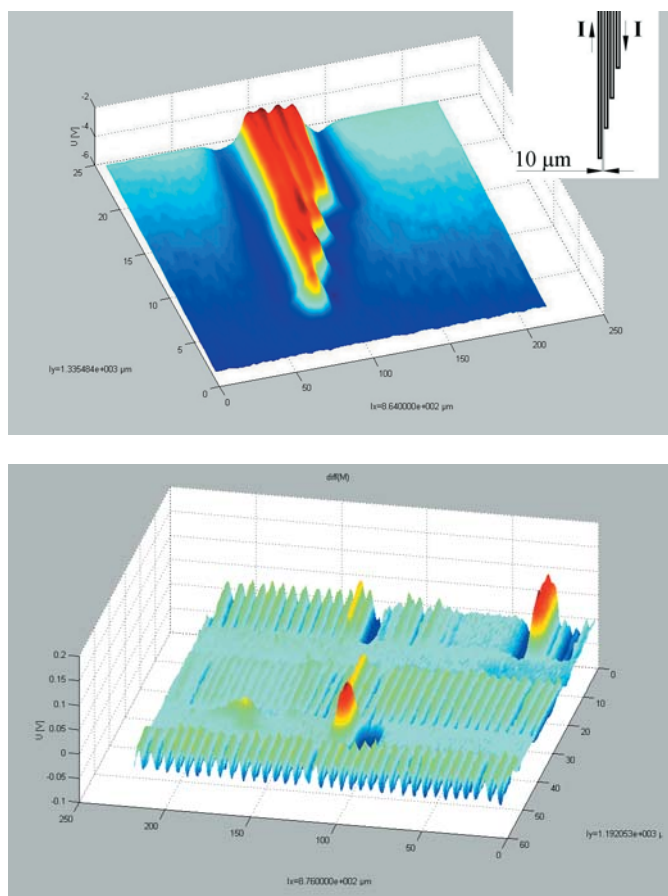


Fig. 4

An example of the measurements of a 2D distribution of magnetic field above a thin-film current-carrying meander, which has 10 μm wide lines separated at 10 μm distance from each other (a) and of magnetic field above a floppy disk (b). Both objects were placed at room temperature outside cryostat. The measurements were performed with a SQUID microscope, developed by IFF and ZEL FZJ.

SQUID microscope

The development of the SQUID systems in Jülich has achieved a level, which allows their application in laboratory prototypes [3]. A limited test production and characterization of custom high- T_c SQUID sensors and SQUID-based measurement systems is a significant part of the development process.

Compared to other magnetic evaluation methods for microscopic objects the scanning SQUID microscope has higher magnetic field sensitivity and a high linearity over a dynamic range up to about 200 dB. Different SQUID microscope measurement systems are presently under study in IFF (see Fig.4). The goal of this research activity is a creation of a new generation of the high- T_c SQUID microscopes with an improved space resolution and sensitivity for room temperature samples. Minimizing SQUID-sam-



ple separation for a better field- and spatial resolution becomes a problem for room temperature objects, which are placed outside the cryostat. The typical separation between the SQUID sensor tip (like one presented in Fig.4) and the room temperature sample is about 100 μm . This relatively large distance limits the space resolution of such type of SQUID microscope to about 50 μm (Neocera). Application of specially designed magnetic flux conductors helps to improve the spacial resolution to submicrometer values.

Development and characterization of custom high- T_c SQUID sensors and SQUID-based measurement systems (e.g., SQUID microscope) occurs also in cooperation with Zentrallabor für Elektronik FZJ (E.Zimmermann, W.Glaas, H.Halling) as well as with international partners like Tristan Technologies Inc. (San Diego, CA, U.S.A.) and the Institute of Radio Engineering & Electronics of Russian Academy of Science (Moscow, Russia).

REFERENCES

- (1) "Low noise HTS dc-SQUID flip-chip magnetometers and gradiometers"
M. I. Faley, U. Poppe, K. Urban, D. N. Paulson, T. N. Starr, and R. L. Fagaly
IEEE Transactions on Appl. Supercond., 11(1), (2001) 1383-1386.
- (2) "Operation of high-temperature superconductor magnetometer with submicrometer bicrystal junctions"
M. I. Faley, U. Poppe, K. Urban, V. Yu. Slobodchikov, Yu. V. Maslennikov, A. Gapelyuk, B. Sawitzki, and A. Schirdewan
Appl. Phys. Lett., 81(13), (2002) 2406-2408.
- (3) "Sensitive HTS gradiometers for magnetic evaluation applications"
M. I. Faley, U. Poppe, K. Urban, D. N. Paulson, T. N. Starr, and R. L. Fagaly
Physica C: Superconductivity, v.372-376, (2002) 217-220.

AUTHORS

Michael I. Faley, Ulrich Poppe, Knut Urban

Terahertz Hilbert Spectroscopy Using Nanoscale High- T_c Josephson Junctions

The principle of Hilbert spectroscopy (HS) [1] is based on the ac Josephson effect in superconducting junctions. If a Josephson junction is irradiated, the electrical response $H(V)$ of a Josephson junction is proportional to the Hilbert-transform of the spectrum $S(f)$ of the incident radiation. Applying an inverse Hilbert transformation to the measured response $H(V)$, allows to recover the spectrum $S(f)$:

$$S(f) = \left(\frac{1}{\pi}\right) \cdot P \int_{-\infty}^{\infty} \frac{H(f_j) \cdot df_j}{f_j - f}$$

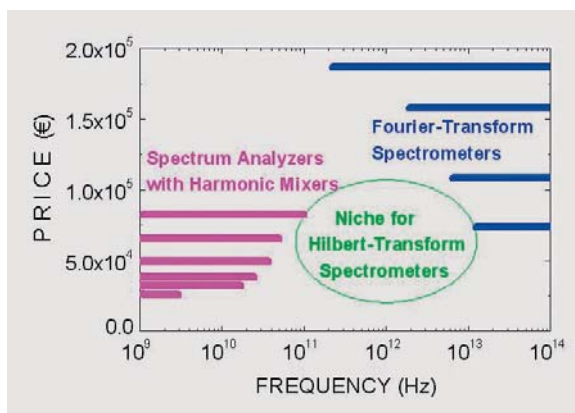
where $f_j = 2eV/\hbar$. Hilbert-transform spectroscopy is similar to Fourier-transform spectroscopy (FS). However, there is an important distinction: in HS a direct transformation of the spectrum into an electrical signal is achieved by a nanoelectronic device, a Josephson junction, while in FS this procedure requires a bulk optical-mechanical device, an interferometer, together with a broadband detector.

The simplicity of HS together with its broad bandwidth, high sensitivity and the short time constant of Josephson junctions might even result in commercial success. The spectrum analyzers and spectrometers based on the conventional techniques are very expensive, if their operational frequencies are extended from their traditional ranges to the intermediate range of millimeter- and submillimeter-waves (see Fig. 1). In the intermediate frequency range from tens of GHz to several THz there is definitely a niche for Hilbert-Transform Spectroscopy.

INTRODUCTION

Fig. 1

Price vs. frequency range for conventional spectroscopic techniques and Hilbert spectroscopy.



APPROACH

We are developing high- T_c Josephson junctions for the Hilbert spectroscopy application in the terahertz range. Starting from the fabrication of high- T_c thin-films, we develop the high- T_c junctions. We study the correlation of the nanostructure, revealed by Atomic Force Microscopy and High-Resolution Electron Microscopy, with the local electrical transport in these junctions and analyse the relation between the nanostructure and the electrical THz response.

RESULTS

High- T_c grain-boundary junction

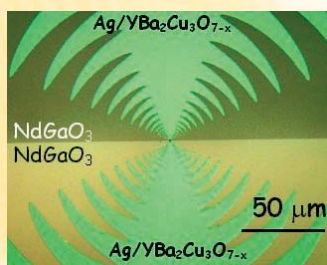


Fig. 2

$\text{YBa}_2\text{Cu}_3\text{O}_{7-x}$ grain-boundary Josephson junction with integrated broadband antenna for Hilbert spectroscopy.

The main part in the Hilbert spectroscopy is a Josephson junction described by an idealized RSJ model. To be useful in the THz range, the junctions should have characteristic voltages $I_c R_n$ exceeding 1 mV. Due to the high value of the energy gap in high- T_c superconductors (20-60 meV), the high- T_c Josephson junctions with the $I_c R_n$ - values exceeding 1 mV are better described by the RSJ model than the low- T_c junctions. Among the different types of high- T_c junctions, the grain-boundary junctions are found to be best characterized by the RSJ model. The micrograph of one of our high- T_c junctions developed for Hilbert spectroscopy is shown in Fig.2. The $I_c R_n$ -values of RSJ-type junctions are up to 0.34 mV at 77 K and up to 2 mV at 35 K.

Spectral range of Hilbert spectroscopy

The spectral range of the Hilbert spectroscopy scales with the $I_c R_n$ -values. For $I_c R_n$ -values of 1.5 mV it reaches THz frequencies at low temperatures (Fig. 3). A high-frequency limit of 4.25 THz has been achieved and a spectral resolution $\delta f/f$ of 10^{-3} demonstrated [2]. Presently we are investigating the THz response of junctions with $I_c R_n$ -values up to 8 mV [3].

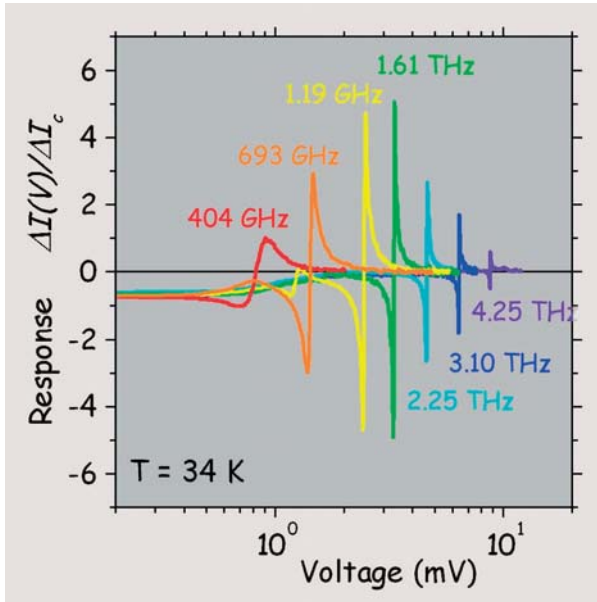


Fig. 3
Spectral range of the Hilbert spectroscopy using $\text{YBa}_2\text{Cu}_3\text{O}_{7-x}$ grain-boundary Josephson junction at 34 K.

Application

Several prototypes of Hilbert spectrometers have been developed and tested in collaboration with the Institute of Radio Engineering & Electronics of Russian Academy of Sciences (Moscow, Russia), Central Electronics Laboratory of Research Center Juelich and TESLA Test Facility at DESY (Hamburg). We have successfully measured the following emission signals: Lorentz spectra of Josephson oscillations, the high harmonic contents of commercial millimeter-wave oscillators, radiation from optically-pumped far-infrared gas lasers and the coherent transition radiation from relativistic electron bunches at the TESLA test facility (DESY, Hamburg) [2]. The interest in THz

Fig. 4

A Hilbert spectrometer, using an optical cryostat. Other designs use Stirling coolers.



analysis is growing due to the development of optical THz quantum cascade lasers, and due to new subterahertz transistors for high-speed logic.

REFERENCES

- [1] Y.Y. Divin, O.Y. Polyanski, A.Y. Shul'man
"Incoherent radiation spectroscopy by means of ac Josephson effect". Sov. Tech. Phys. Lett., v. 6, pp. 454-458, 1980.
- [2] Y. Divin, O. Volkov, V. Pavlovskii, V. Shiroto, P. Shadrin, U. Poppe, K. Urban
"Terahertz Hilbert spectroscopy by high- T_c Josephson junctions." In Advances in Solid State Physics, 41, ed. B. Kramer (Springer, Berlin, 2001) pp. 301-313.
- [3] Y.Y. Divin, U. Poppe, C.L. Jia, P.M. Shadrin, K. Urban
"Structural and electrical properties of $\text{YBa}_2\text{Cu}_3\text{O}_{7-x}$ [100]-tilt grain boundary Josephson junctions with large $I_c R_n$ -product on SrTiO_3 bicrystals." Physica C, vol. 372-376, pp. 115-118, 2002.

AUTHORS

Yuri Y. Divin, Ulrich Poppe, Knut Urban



